OPEN ACCESS

KING'S College LONDON

King's Research Portal

DOI:
10.1016/j.media.2017.12.005

Document Version
Peer reviewed version

Link to publication record in King's Research Portal

Citation for published version (APA):
Fovargue, D., Kozerke, S., Sinkus, R., & Nordsletten, D. (2017). Robust MR elastography stiffness quantification using a localized divergence free finite element reconstruction. *Medical Image Analysis*, *44*, 126-142. https://doi.org/10.1016/j.media.2017.12.005

Citing this paper
Please note that where the full-text provided on King's Research Portal is the Author Accepted Manuscript or Post-Print version this may differ from the final Published version. If citing, it is advised that you check and use the publisher's definitive version for pagination, volume/issue, and date of publication details. And where the final published version is provided on the Research Portal, if citing you are again advised to check the publisher's website for any subsequent corrections.

General rights
Copyright and moral rights for the publications made accessible in the Research Portal are retained by the authors and/or other copyright owners and it is a condition of accessing publications that users recognize and abide by the legal requirements associated with these rights.

•Users may download and print one copy of any publication from the Research Portal for the purpose of private study or research.
•You may not further distribute the material or use it for any profit-making activity or commercial gain
•You may freely distribute the URL identifying the publication in the Research Portal

Take down policy
If you believe that this document breaches copyright please contact librarypure@kcl.ac.uk providing details, and we will remove access to the work immediately and investigate your claim.

Download date: 05. May. 2023

Accepted Manuscript

Robust MR elastography stiffness quantification using a localized divergence free finite element reconstruction

Daniel Fovargue, Sebastian Kozerke, Ralph Sinkus, David Nordsletten

PII: S1361-8415(17)30187-1
DOI: 10.1016/j.media.2017.12.005
Reference: MEDIMA 1325

To appear in: *Medical Image Analysis*

Received date: 19 May 2017
Revised date: 10 October 2017
Accepted date: 4 December 2017

Please cite this article as: Daniel Fovargue, Sebastian Kozerke, Ralph Sinkus, David Nordsletten, Robust MR elastography stiffness quantification using a localized divergence free finite element reconstruction, *Medical Image Analysis* (2017), doi: 10.1016/j.media.2017.12.005

This is a PDF file of an unedited manuscript that has been accepted for publication. As a service to our customers we are providing this early version of the manuscript. The manuscript will undergo copyediting, typesetting, and review of the resulting proof before it is published in its final form. Please note that during the production process errors may be discovered which could affect the content, and all legal disclaimers that apply to the journal pertain.

ACCEPTED MANUSCRIPT

Highlights

- A local direct reconstruction method for MR elastography is proposed.
- The method is parameterless and is shown to be accurate, robust, and fast.
- Comparisons are made with two state of the art methods over multiple data sets.
- A noise sensitivity analysis is performed on the methods to profile robustness.

ACCEPTED MANUSCRIPT

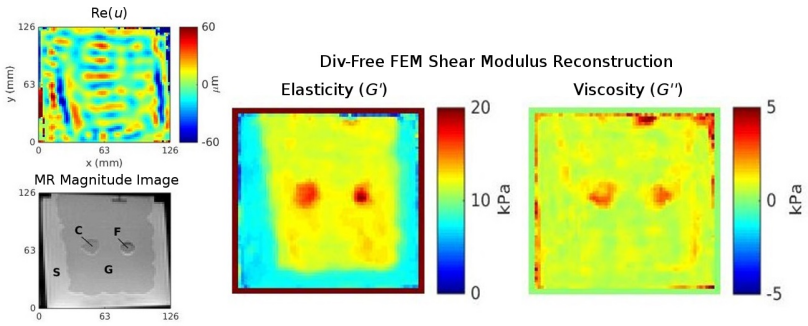

ACCEPTED MANUSCRIPT

ACCEPTED MANUSCRIPT

Robust MR elastography stiffness quantification using a localized divergence free finite element reconstruction

Daniel Fovargue[a], Sebastian Kozerke[b], Ralph Sinkus[a], David Nordsletten[a]

[a] *Division of Imaging Sciences and Biomedical Engineering, King's College London, London, United Kingdom*
[b] *Institute for Biomedical Engineering, University and ETH Zürich, Zürich, Switzerland*

Abstract

As disease often alters structural and functional properties in tissue, the noninvasive measurement of material stiffness *in vivo* is desirable. Magnetic resonance elastography provides an approach to *in vivo* tissue characterization, using images of wave motion in tissue and biomechanical principles to reconstruct and quantify stiffness. Successful clinical translation of this technology requires stiffness reconstruction algorithms that are robust, easy to manage, and fast. In this paper, a reconstruction method is presented which addresses these issues by using a local compact divergence-free reconstruction kernel coupled with non-physical constraint elimination and inverse residual weighting to reliably reconstruct stiffness. The proposed technique is compared with local curl reconstructions and global stiffness-pressure reconstructions across two ground-truth phantoms as well as in vivo data sets. Sensitivity analysis is also performed, assessing the variability of reconstruction results and robustness to noise. It is shown that the proposed method can be robustly applied across data sets, is less sensitive to noise, attains comparable (or improved) accuracy, provides better correlation to anatomical features, and can be completed in short timescales.

Keywords: MR Elastography, Reconstruction, Shear modulus, Tissue Biomechanics, Inverse Problem, Stiffness

ACCEPTED MANUSCRIPT

ACCEPTED MANUSCRIPT

1. Introduction

Tissue stiffness is considered a valuable clinical marker as abnormalities - such as tumors, inflamation, or fibrosis - can fundamentally alter tissue structure, leading to significant variations in material properties. In the case of tumors, factors such as angiogenesis, increase in cell stiffness, and compaction of surrounding tissue alter homeostatic conditions (Krouskop et al., 1998; Paszek et al., 2005). In liver fibrosis, scarring occurs in the liver, yielding an increased collagen density in the extracellular matrix (Bataller and Brenner, 2005; Yeh et al., 2002). Clinical evaluation of tissue properties is commonly accomplished through palpation or invasive biopsy procedures (Mariappan et al., 2010). Both techniques remain limited, with palpation applicable to superficial tissues and biopsy to conditions serious enough to warrant an invasive test.

Leveraging modern imaging and engineering, magnetic resonance elastography (MRE) provides an alternative approach to tissue stiffness characterization that is quantitative and non-invasive (Glaser et al., 2012). MRE uses phase contrast imaging to record a full three dimensional field of displacements in tissue induced by a transducer (a common approach is harmonic MRE which employs a single-frequency vibration) (Parker et al., 2011). The recorded data represents movement of mechanical waves and, by employing a reconstruction algorithm, the underlying tissue stiffness can be quantified. MRE has been applied to disease areas such as liver fibrosis (Bonekamp et al., 2009; Huwart et al., 2008; Rouvière et al., 2006; Venkatesh et al., 2013; Yin et al., 2007) and breast cancer (McKnight et al., 2002; Sinkus et al., 2000, 2007), and to other organs such as brain (Green et al., 2008; Kruse et al., 2008; Sack et al., 2007) (including Alzheimer's (Murphy et al., 2011) and cancer (Jamin et al., 2015)), prostate (Kemper et al., 2004; Li et al., 2011; Sahebjavaher et al., 2013), and heart (Kolipaka et al., 2010; Sack et al., 2009) among others (Glaser et al., 2012; Mariappan et al., 2010). As MRE continues to become more widely used, both clinically and in research, it is critical to provide reconstruction algorithms that are robust, accurate, easy-to-use, and can be completed in clinical time scales.

ACCEPTED MANUSCRIPT

MRE reconstruction is considered an inverse problem, as the given wave behavior depends on the unknown stiffness distribution, which must be computed. Due to the small displacements associated with the waves, the linear viscoelastic wave equation (LVWE) is typically assumed to accurately model the wave behavior (Glaser et al., 2012). Reconstruction methods based on the LVWE can be split into two main categories - *direct* and *iterative* - that vary fundamentally in principle. Direct methods assume that the wave behavior measured from MR is sufficiently accurate that insertion into the governing equations (e.g. LVWE) leaves the stiffness distribution as the principal unknown and can be found by error minimization. These methods are therefore inherently sensitive to data quality.

In contrast, iterative techniques most often seek to solve a forward problem and iteratively adapt stiffness parameters in order to minimize the difference between the resultant forward solution and measured wave field. As a result, iterative methods tend to be less sensitive to noise, but strongly dependent on the forward problem and the assumption that it correctly models the wave behavior. Inconsistency here may lead to incorrect solutions or even divergence. Therefore these methods are potentially more biased by model assumptions (such as the governing equations, initial stiffness distributions, boundary conditions, etc). Furthermore, iterative methods are typically more computationally expensive than direct methods, as they require many solutions to the forward instead of acting directly on the data. For some examples of iterative methods see Eskandari et al. (2008); Miga (2003); Oberai et al. (2003); Van Houten et al. (2001); Zhang et al. (2006) and for a comparison of iterative and direct methods see Honarvar et al. (2016). As the focus here includes ease of use and processing within clinical time scales, iterative methods will not be considered, as currently these are computationally expensive methods that can require expert knowledge to execute.

Direct methods can be further subdivided into two general types of approaches. The first type are *global* methods, where the stiffness is considered to have spatial variability and reconstructions are performed over the entire re-

ACCEPTED MANUSCRIPT

gion of interest (ROI) (Eskandari et al., 2011; Guo et al., 2010; Honarvar et al., 2012, 2013; Park and Maniatty, 2006, 2009; Zhu et al., 2003). The second type are *local* methods, where the stiffness is taken to be constant locally and many small independent reconstructions are performed which eventually span the ROI (Bercoff et al., 2003; Connesson et al., 2015; Manduca et al., 2003; McLaughlin et al., 2006; Okamoto et al., 2011; Oliphant et al., 2001; Romano et al., 1998; Sinkus et al., 2005b) . Some local methods fit or utilize properties of known solutions of the wave equation instead of directly solving the equations (Baghani et al., 2011; Tzschätzsch et al., 2016). Local methods are less accurate in areas which contain significant stiffness heterogeneity, whereas global methods are more computationally expensive and typically require tuning of regularization parameters. Many previous comparisons and descriptions of global methods are limited to *in silico* and phantom data, so the robustness of these methods when reconstructing complex anatomical data has not been well established. Here, both local and global methods are considered and comparisons between them are shown, including on anatomical data sets, such as breast and brain.

In addition to these comparisons, this paper presents a novel, computationally inexpensive, robustand easy-to-use method for MRE reconstruction. The proposed reconstruction is local in the sense described above and uses a compact finite element method (FEM) reconstruction kernel of the LVWE with specialized divergence-free projections to eliminate unknown tractions and hydrostatic forces. Additional techniques for reducing noise effects, increasing accuracy, and mitigating the drawbacks of the local homogeneity assumption are also described. The proposed reconstruction is compared to two state-of-the-art methods: a local curl-based approach (Sinkus et al., 2005b) and a global FEM approach (Park and Maniatty, 2006; Honarvar et al., 2012), both of which have been used in recent scientific work (Garteiser et al., 2012; Runge et al., 2014; Sahebjavaher et al., 2014, 2015; Schregel et al., 2012). To verify the methods, two phantom data sets with known viscoelastic properties are reconstructed. A sensitivity analysis is then presented that incorporates several different tests to investigate the effects of noise on the performance of the reconstruction tech-

ACCEPTED MANUSCRIPT

niques. Finally, anatomical data sets are reconstructed in order to evaluate efficacy *in vivo*. Methods are compared by correlation of stiffness to anatomy and consistency over multiple simultaneous scans. Results show that the proposed method has improved stability and robustness, comparable or improved accuracy, and maintains a low computing time.

In Section 2, theory is presented and the proposed div-free FEM reconstruction method is described along with the two comparison methods. In Section 3, the methods are verified using two phantom data sets, a noise sensitivity analysis is performed, and the methods are applied to multiple anatomical data sets. A discussion of these comparisons and results is provided in Section 4 and conclusions are made in Section 5.

2. Methods

The mechanical waves induced in tissue during harmonic MRE are typically modeled by the LVWE over some 3D ROI or domain, Ω, with boundary Γ. Under the time harmonic assumption, the displacements and hydrostatic stress are complex-valued functions of space, $\mathbf{u} = \mathbf{u}(\mathbf{x})$ and $p = p(\mathbf{x})$, respectively, where $\mathbf{x} \in \Omega$. These are related to the physical time-dependent real-valued functions via $\mathbf{u}_r(\mathbf{x}, t) = \mathrm{Re}\,[\mathbf{u}(\mathbf{x})\exp(i\omega t)]$ and $p_r(\mathbf{x}, t) = \mathrm{Re}\,[p(\mathbf{x})\exp(i\omega t)]$. This assumption leads to the following equations:

$$\rho\omega^2\mathbf{u} + \nabla\cdot(GD\mathbf{u}) + \nabla p = \mathbf{0} \quad \text{on} \quad \Omega \tag{1}$$

$$\nabla\cdot\mathbf{u} - \frac{p}{\lambda} = 0 \quad \text{on} \quad \Omega \tag{2}$$

$$\mathbf{u} = \hat{\mathbf{u}} \quad \text{on} \quad \Gamma_1 \tag{3}$$

$$(GD\mathbf{u} + p\mathbf{I})\cdot\mathbf{n} = \hat{\mathbf{T}} \quad \text{on} \quad \Gamma_2, \tag{4}$$

where $D\mathbf{u} = \nabla\mathbf{u} + (\nabla\mathbf{u})^T$, $\lambda(\mathbf{x})$ is the complex-valued first Lamé parameter, $G(\mathbf{x})$ is the complex-valued shear modulus, $\rho(\mathbf{x})$ is the material density, ω is the angular frequency, and $\Gamma = \Gamma_1 \bigcup \Gamma_2$. Equations (3) and (4) reference the boundary conditions where known displacements, $\hat{\mathbf{u}}$, are imposed on Γ_1 and known tractions, $\hat{\mathbf{T}}$, on Γ_2 with the unit vector normal to Γ_2 denoted as $\mathbf{n}$.

ACCEPTED MANUSCRIPT

The shear modulus, G, is often split into real and imaginary components, i.e. $G = G' + iG''$, where G' is the storage modulus and G'' is the loss modulus. For tissue, the density is usually considered to be constant and equal to the density of water, i.e. $\rho(\mathbf{x}) = 1000 \text{ kg/m}^3$.

In a typical forward solution to (1)-(4), the material parameters, ρ, λ, and G, as well as ω and sufficient boundary conditions are given while $\mathbf{u}$ and p are unknown. In the case of MRE reconstruction, an inverse solution is necessary, since $\mathbf{u}$ is given from measured data. Density and angular frequency, ρ and ω, remain known and so this leaves the stiffness, λ and G, and p as unknowns. If it is assumed that λ is not much greater than G or that $\nabla \cdot \mathbf{u}$ can be accurately computed, then (2) can be inserted into (1) and the given $\mathbf{u}$ can be used to reconstruct both λ and G. These properties can not typically be assumed for elastography reconstruction however, as, for tissue, λ is much larger than G. Additionally, $\nabla \cdot \mathbf{u}$ is small so its computation is unreliable due to the noise in $\mathbf{u}$. The value of λ could be set to some large number or, more probably, the Poisson ratio could be set to a value just slightly less than 0.5, leaving only G to be reconstructed (Eskandari et al., 2011; Guo et al., 2010; Zhu et al., 2003). Although λ will be inaccurate, the shear modulus G may be reconstructed accurately; however this may lead to errors in regions with strong mode conversion.

Often tissue is considered incompressible and (2) simplifies to a pure divergence free condition, $\nabla \cdot \mathbf{u} = 0$. In this case, only (1) is solved for G and p. From here, there are three common routes in MRE reconstruction. First, some methods consider the gradient of p to be negligible, simply removing this term from (1) (Bercoff et al., 2003; Manduca et al., 2003; McLaughlin et al., 2006; Oliphant et al., 2001). However, it has been shown that neglecting the pressure term leads to error in stiffness reconstructions (Park and Maniatty, 2006). Another approach is to remove the pressure term by taking the curl of (1),

$$\rho\omega^2 \nabla \times \mathbf{u} + \nabla \times (\nabla \cdot (GD\mathbf{u})) = \mathbf{0} \quad \text{on} \quad \Omega, \tag{5}$$

since the curl of the gradient of a scalar potential is zero (Honarvar et al., 2013; Sinkus et al., 2005b). This increases the order of differentiation of $\mathbf{u}$,

ACCEPTED MANUSCRIPT

requiring increased measurement accuracy to obtain the same reconstruction quality. Alternatively, p may be solved for, in addition to G (Honarvar et al., 2012, 2016; Park and Maniatty, 2006, 2009). This typically requires regularizing p which introduces parameters that may need to be tuned to optimize results.

All of the published reconstruction methods mentioned in this section solve (1), or variants of it, like (5), for stiffness via a direct least squares solution, that is, minimize the discrepancy in the equation. As mentioned in Section 1, these methods are split between global and local, where local methods assume local homogeneity of stiffness. So while global methods solve (1) on Ω, or at least large subregions of Ω, local methods simplify (1) by assuming G is constant and solve on small subregions of Ω, denoted by Ω_L. The two methods used for comparisons (a local curl-based method and a global FEM method that solves for pressure) and the proposed div-free FEM method are described in Sections 2.2, 2.4, and 2.5, respectively.

2.1. Image data

In MRE, 3D displacement data corresponding to waves induced by a single frequency transducer are recorded by MR imaging at several time points along the wave cycle. These are then transformed into a complex valued field based on the time harmonic assumption. As is typical of MR images, the harmonic displacement data are represented on a uniform 3D grid of voxels, which may also be referred to as a stack of images or slices. So, the true continuous displacement field, $\mathbf{u}$, is approximated by the discrete set of MRI obtained values, $\hat{\mathbf{u}}$, and these are related by

$$\hat{\mathbf{u}}(i,j,k) = \mathbf{u}(h_1 i, h_2 j, h_3 k) + \boldsymbol{\epsilon}(h_1 i, h_2 j, h_3 k), \tag{6}$$

where $\boldsymbol{\epsilon}$ represents the error due to discretization, noise, voxel averaging, and other factors, (i,j,k) counts over the voxels in the (x,y,z) directions, respectively, and h_1, h_2, and h_3 are the voxel dimensions. The goal of the reconstruction algorithm is then to provide a stiffness value at each voxel location, $G(i,j,k)$, sometimes called an *elastogram*.

ACCEPTED MANUSCRIPT

Limiting the influence of noise in the MR images is often accomplished by applying a low pass filter such as Gaussian smoothing, which here is included as an optional pre-processing step. Smoothing is applied in a standard three dimensional way by reassigning voxel values based on some chosen convolution kernel. An important feature to recognize in direct methods is that excess noise will tend to lower the reconstructed stiffness, as high frequency waves correspond to soft or low stiffness material. Therefore, smoothing the data tends to increase reconstructed stiffness. An appropriate choice of smoothing depends on the signal-to-noise ratio (SNR) and also the ratio of wavelength to voxel size, as local derivative estimates will be more affected by noise for longer wavelengths.

Noise becomes more problematic when constructing the necessary derivatives of $\hat{\mathbf{u}}$ for insertion in equations (1) and (5) as differentiation tends to amplify noise. Therefore, many published reconstruction methods, and two of the methods developed here, utilize FEM because, as an integration approach, it reduces the order of derivatives. For all three methods, the necessary derivatives of $\hat{\mathbf{u}}$ are precomputed via least squares polynomial fitting (also called Savitzky-Golay filtering (Savitzky and Golay, 1964)). This approach has often been used in MRE reconstruction, for example, in Oliphant et al. (2001), Manduca et al. (2001), Sinkus et al. (2005a), and Honarvar et al. (2012). In Honarvar et al. (2016) this approach is shown to be more stable and accurate than standard FEM calculations of derivatives of $\hat{\mathbf{u}}$. The following notation is introduced:

$$D_{pf}\left(\hat{\mathbf{u}}\left(\mathbf{i}\right);\star\right), \tag{7}$$

which represents the result of applying polynomial fitting to the data, $\hat{\mathbf{u}}$, at voxel $\mathbf{i} = (i, j, k)$, to construct the derivatives required by the operator $\star$. For example, the curl of the data $\hat{\mathbf{q}} = \nabla \times \hat{\mathbf{u}}$ at each voxel will be given by

$$\hat{\mathbf{q}}\left(\mathbf{i}\right) = D_{pf}\left(\hat{\mathbf{u}}\left(\mathbf{i}\right);\nabla\times\right). \tag{8}$$

Only first and third derivatives of $\hat{\mathbf{u}}$ will be required. For first derivatives, a linear 3D polynomial is fit to the $3 \times 3 \times 3$ cube of data centered around each

ACCEPTED MANUSCRIPT

voxel and the derivatives of this polynomial at the voxel are used. For third derivatives, a cubic polynomial is fit to data within a shape approximating a sphere bounded by the surrounding $5 \times 5 \times 5$ cube (the inner $3 \times 3 \times 3$ cube is used along with data from the six $3 \times 3 \times 1$ sections lying on the faces of the inner cube).

2.2. Local curl reconstruction

The local curl-based method is based on (Sinkus et al., 2005b) and is used here for comparison. This reconstruction method solves (5) and assumes G is locally constant. This simplifies (5), which becomes

$$\rho\omega^2\mathbf{q} + G\Delta\mathbf{q} = \mathbf{0}, \tag{9}$$

where $\mathbf{q} = \nabla \times \mathbf{u}$. Required derivatives are found by polynomial fitting, so at each voxel, $\mathbf{i}$, the discretized equation is,

$$\rho\omega^2\hat{\mathbf{q}}(\mathbf{i}) + G(\mathbf{i})\,\hat{\Delta\mathbf{q}}(\mathbf{i}) = \mathbf{0}, \tag{10}$$

where $\hat{\Delta\mathbf{q}}(\mathbf{i}) = D_{pf}(\hat{\mathbf{u}}(\mathbf{i}); \Delta\nabla\times)$ and $\hat{\mathbf{q}}(\mathbf{i})$ is given by (8). Equation (10) is solved for $G(\mathbf{i})$ via least squares, where there are three complex equations for each complex valued $G(\mathbf{i})$,

$$G(\mathbf{i}) = -\rho\omega^2 \frac{(\hat{\Delta\mathbf{q}}(\mathbf{i}))^T(\hat{\mathbf{q}}(\mathbf{i}))}{(\hat{\Delta\mathbf{q}}(\mathbf{i}))^T(\hat{\Delta\mathbf{q}}(\mathbf{i}))}. \tag{11}$$

2.3. FEM based reconstruction

As mentioned previously, FEM is a common numerical approach in MRE reconstruction (Romano et al., 1998; Van Houten et al., 2001; Park and Maniatty, 2006; Eskandari et al., 2011; Honarvar et al., 2012). Here, it is employed by both the proposed local method and the global method. FEM implementations operate on the weak (or variational) form of equations. The general weak form is essentially standard across FEM-based MRE reconstruction, typically only varying as much as the strong form equations (e.g., homogeneity assumption, compressibility, application of curl). Prior FEM-based MRE reconstruction

ACCEPTED MANUSCRIPT

methods and the two developed here have varying implementation details including element type, numerical integration, and, in the case of local methods, support size. For example, Romano et al. (1998) consider the weak form of the compressible equations, use cubic interpolation of displacement data, and perform numerical integration to create three equations to solve at each voxel for stiffness. Van Houten et al. (2001) consider the compressible equations and use linear triangular elements while utilizing FEM to solve forward problems within a global iterative approach. Connesson et al. (2015) present a virtual fields method starting from the virtual work form of the equations (equivalent to the weak form after integration by parts) and a local reconstruction is performed at each voxel using a mesh formed from linear hexahedral elements. Here, the proposed method considers the incompressible formulation, utilizes linear approximations to reduce noise sensitivity in an inf-sup stable element, constructs a local mesh (approximating a spherical shape) to increase the number of constraints per unknown, and incorporates various other improvements discussed later.

The weak form of the incompressible versions of (1)-(2) are found from multiplying by test functions, $\mathbf{w}$ and q, and integrating. The forward problem becomes: Find $(\mathbf{u}, p) \in \mathcal{U} \times L^2_{\mathbb{C}}(\Omega)$ such that for all $(\mathbf{w}, q) \in \mathcal{U}_0 \times L^2_{\mathbb{C}}(\Omega)$

$$\int_\Omega \left(\rho\omega^2 \mathbf{u}\cdot\mathbf{w} - GD\mathbf{u} : \nabla\mathbf{w} - p\,\nabla\cdot\mathbf{w}\right) \mathrm{d}\Omega + \int_{\Gamma_2} \hat{\mathbf{T}}\cdot\mathbf{w}\,\mathrm{d}\Gamma_2 = 0 \qquad (12)$$

$$\int_\Omega q\,\nabla\cdot\mathbf{u}\,\mathrm{d}\Omega = 0, \qquad (13)$$

with the trial function space $\mathcal{U} = \left\{\mathbf{u} | \mathbf{u} \in H^1_{\mathbb{C}}(\Omega), \mathbf{u} = \hat{\mathbf{u}} \text{ on } \Gamma_1\right\}$ and the test function space $\mathcal{U}_0 = \left\{\mathbf{w} | \mathbf{w} \in H^1_{\mathbb{C}}(\Omega), \mathbf{w} = \mathbf{0} \text{ on } \Gamma_1\right\}$.

From here, the equations are discretized based on element choice and corresponding shape functions. A superscript h will denote these finite dimensional approximations of continuous functions, e.g. $\mathbf{u}^h$, so that equations (12) and (13)

ACCEPTED MANUSCRIPT

become

$$\int_\Omega \left(\rho\omega^2 \mathbf{u}^h \cdot \mathbf{w}^h - G^h D\mathbf{u}^h : \nabla \mathbf{w}^h - p^h \nabla \cdot \mathbf{w}^h\right) \mathrm{d}\Omega + \int_{\Gamma_2} \hat{\mathbf{T}} \cdot \mathbf{w}^h \, \mathrm{d}\Gamma_2 = 0 \quad (14)$$

$$\int_\Omega q^h \nabla \cdot \mathbf{u}^h \, \mathrm{d}\Omega = 0, \quad (15)$$

Here, the finite dimensional functions are linear combinations of nodal-Lagrange shape functions

$$G^h = \sum_{l=1}^{N_G} G_l \, \psi_l^G(\mathbf{x}) \quad (16)$$

$$\mathbf{u}^h = \sum_{l=1}^{N_u} \mathbf{u}_l \, \psi_l^u(\mathbf{x}) \quad (17)$$

$$\mathbf{w}^h = \sum_{l=1}^{N_w} \mathbf{w}_l \, \psi_l^u(\mathbf{x}) \quad (18)$$

$$p^h = \sum_{l=1}^{N_p} p_l \, \psi_l^p(\mathbf{x}) \quad (19)$$

$$q^h = \sum_{l=1}^{N_q} q_l \, \psi_l^p(\mathbf{x}) \,, \quad (20)$$

where N_* are the number of nodes, ψ_l^* are the shape functions corresponding to node l for each variable, $*$, and G_l, $\mathbf{u}_l$, $\mathbf{w}_l$, p_l, and q_l are the values of the variables at node l. The shape functions are polynomials with value 1 at their associated node and 0 at all other nodes.

For the inverse problem, the displacements are given, so nodal values are found by $\mathbf{u}_l = \hat{\mathbf{u}}(\mathbf{i}_l)$, where $\mathbf{i}_l$ is the voxel at node l. Typically, in FEM, derivatives of the variables would be computed by taking derivatives of the shape functions. As mentioned above though, it is preferable with this type of data for derivatives to be computed by polynomial fitting. So, within the FEM, $\nabla\mathbf{u}$ is considered a separate variable and is interpolated via

$$(\nabla\mathbf{u})^h = \sum_{l=1}^{N_{\nabla u}} (\nabla\mathbf{u})_l \, \psi_l^u(\mathbf{x}) \,, \quad (21)$$

with nodal values given by

$$(\nabla\mathbf{u})_l = D_{pf}\left(\hat{\mathbf{u}}(\mathbf{i}_l); \nabla\right). \quad (22)$$

ACCEPTED MANUSCRIPT

Also, equation (15) is ignored, as the displacements are known. Finally, since tractions are unknown, the test function space is amended so that the traction term in equation (14) is removed. This is accomplished by having the test functions be zero on the entire boundary, $\mathcal{V}_0 = \left\{\mathbf{w} | \mathbf{w} \in H^1_{\mathbb{R}}(\Omega), \mathbf{w} = \mathbf{0} \text{ on } \Gamma\right\}$ (Romano et al., 1998; Park and Maniatty, 2006). This has the effect of removing all equations associated with boundary nodes. In a typical FEM problem, these equations would be replaced by Dirichlet boundary conditions, but this cannot be done for the stiffness as it is completely unknown, and so the equations are lost. The methods here are implemented so that enough equations will remain in order to determine the unknown stiffness.

2.4. Global heterogeneous reconstruction

The global FEM method developed here is based on some described in literature (Eskandari et al., 2011; Honarvar et al., 2012; Park and Maniatty, 2006), differing only by element choice and regularization, and so is presumed to show essentially equivalent behavior. As a global method, this approach considers G to be a function of space and solves (14) over the whole domain or ROI, Ω. In practice, some global methods are applied to subsets of Ω but these subsets are significantly larger than the subsets used for local methods. The matrix system corresponding to (14), including the modified test function space, $\mathcal{V}_0$, is

$$\mathbf{KG} + \mathbf{CP} = \rho\omega^2\mathbf{MU}, \tag{23}$$

where $\mathbf{G} = (G_1, G_2, \ldots, G_{N_G})^T$, $\mathbf{P} = (P_1, P_2, \ldots, P_{N_P})^T$, $\mathbf{U} = \left(\mathbf{U}_x^T, \mathbf{U}_y^T, \mathbf{U}_z^T\right)^T$, and $\mathbf{U}_k = \left(\hat{u}_k(\mathbf{i}_1), \hat{u}_k(\mathbf{i}_2), \ldots, \hat{u}_k(\mathbf{i}_{N_u})\right)^T$ The matrices $\mathbf{K}$, $\mathbf{C}$, and $\mathbf{M}$ are constructed in a standard way, detailed in Appendix A.

For the global reconstruction, the inf-sup stable hexahedral $\mathbb{Q}^2$-$\mathbb{Q}^1$ element (Hughes, 2000) is used, in which the displacements, test functions, and stiffness are represented by quadratic shape functions and the pressure is represented by linear shape functions. In Park and Maniatty (2006) and Honarvar et al. (2012) a combination of linear and discontinuous constant shape functions are used. Regularization of the stiffness and pressure is also required for the global ap-

ACCEPTED MANUSCRIPT

proach. A Tikhonov regularization method (Tikhonov et al., 1995) is employed by adding the Laplacian of G and p to the equations to be minimized, as well as a term to minimize p itself, resulting in

$$\begin{pmatrix} \mathbf{K}^T\mathbf{K} + \alpha_G \mathbf{D}_G^T \mathbf{D}_G & \mathbf{K}^T\mathbf{C} \\ \mathbf{C}^T\mathbf{K} & \mathbf{C}^T\mathbf{C} + \alpha_{p1}\mathbf{I}_p + \alpha_{p2}\mathbf{D}_p^T\mathbf{D}_p \end{pmatrix} \begin{pmatrix} \mathbf{G} \\ \mathbf{P} \end{pmatrix} = \rho\omega^2 \begin{pmatrix} \mathbf{K}^T\mathbf{M}\mathbf{U} \\ \mathbf{C}^T\mathbf{M}\mathbf{U} \end{pmatrix} \tag{24}$$

after applying least squares. The matrices $\mathbf{D}_G$ and $\mathbf{D}_p$ represent finite difference discretizations of the Laplacian for G and p, respectively, α_G, α_{p1} and α_{p2} are the regularization weighting parameters, and $\mathbf{I}_p$ is an identity matrix. The pressure regularization parameter, α_{p1}, must be nonzero to avoid poor conditioning.

In Park and Maniatty (2006), the pressure regularization is the same as here, whereas a stiffness regularization is not specified. In Honarvar et al. (2012), sparsity regularization of the stiffness and pressure is used, and while this is shown to provide more accuracy in simulations, it is stated that similar quality results can be obtained by either Tikhonov or sparsity regularization in phantom data. Tikhonov regularization is chosen here because the sparse and banded properties of the matrix system are preserved leading to a faster and less memory intensive inversion.

2.5. Proposed reconstruction

As in the local curl method, the proposed method assumes local homogeneity of stiffness over small subregions, Ω_L, of Ω with boundaries Γ_L. Therefore, G is considered to be constant so can be taken out of the integral and will not be represented by shape functions. The weak form problem (12)-(13) is further modified by changing the test function space to only consider divergence-free functions, $\tilde{\mathcal{V}}_0 = \left\{ \mathbf{w} | \mathbf{w} \in H^1_{\mathbb{R}}(\Omega_L), \int_{\Omega_L} q \, \nabla \cdot \mathbf{w} \, \mathrm{d}\Omega_L = 0 \; \forall q \in L^2_{\mathbb{C}}(\Omega_L), \mathbf{w} = \mathbf{0} \text{ on } \Gamma_{2,L} \right\}$, which removes the pressure term. Equation (14) becomes

$$\int_{\Omega_L} \left(\rho\omega^2 \mathbf{u}^h \cdot \mathbf{w}^h - G \nabla \mathbf{u}^h : \nabla \mathbf{w}^h - G \left(\nabla \cdot \mathbf{u}^h \right) \left(\nabla \cdot \mathbf{w}^h \right) - p^h \, \nabla \cdot \mathbf{w}^h \right) \mathrm{d}\Omega_L = 0, \tag{25}$$

which is written in matrix form as

$$\rho\omega^2 \tilde{\mathbf{M}}\mathbf{U} - G\tilde{\mathbf{K}}\nabla\mathbf{U} - G\tilde{\mathbf{C}}\nabla \cdot \mathbf{U} - \tilde{\mathbf{C}}\mathbf{P} = \mathbf{0}, \tag{26}$$

ACCEPTED MANUSCRIPT

where $\nabla\mathbf{U}$ is a vector containing all displacement derivatives at every node, $\nabla \cdot \mathbf{U}$ is a vector containing the divergence of the displacements at every node, the tildes represent use of $\tilde{\mathcal{V}}_0$, and, because of this test function space, $\tilde{\mathbf{C}}$ is zero. In practice, the matrices in (26) are constructed by first forming matrices using standard test functions from $\mathcal{V}_0$, which, as in the global method, are denoted $\mathbf{M}$, $\mathbf{K}$, $\mathbf{C}$. To enforce the divergence-free constraint on the test functions, the matrix $\mathbf{X} = \text{null}(\mathbf{C}^T)$ is constructed. Hence, equation (26) is first calculated from

$$\rho\omega^2\mathbf{X}^T\mathbf{M}\mathbf{U} - G\mathbf{X}^T\mathbf{K}\nabla\mathbf{U} = \mathbf{0} \tag{27}$$

and becomes

$$\rho\omega^2\tilde{\mathbf{M}}\mathbf{U} - G\tilde{\mathbf{K}}\nabla\mathbf{U} = \mathbf{0}. \tag{28}$$

The construction of the matrices $\mathbf{M}$, $\mathbf{K}$, and $\mathbf{C}$ is detailed in Appendix A. Connesson et al. (2015) incorporate removal of the compressional term into the conditions imposed on an optimized virtual field and so is similar to the approach described here. However, in that work, a single optimal field is found, whereas here the solution is found from minimizing over the space of divergence-free test functions, and further, inf-sup stability is not considered.

Unlike taking the curl of the equations, using weakly divergence-free test functions to remove the pressure term does not directly remove the compressional component of the waves. In fact, in terms of the final stiffness result, it is similar to solving for the pressure. It does, however, reduce the system size and therefore computational cost, although this is only true when computing on small local domains. Since the matrix $\mathbf{X}^T$ is full, the normally banded system is replaced with a full system. For small systems, as in a local solution, it makes little difference if the system is full or sparse, but for larger systems resulting from a global reconstruction, a full matrix inversion will be much more computationally expensive than a sparse inversion. Additionally, removing the pressure term simplifies the structure of the equation making some of the improvements discussed later more straightforward to justify and implement.

As in the local curl method, the proposed method works one voxel at a time,

ACCEPTED MANUSCRIPT

computing a single complex value of stiffness. It solves equation (28) via least squares,

$$G(\mathbf{i}) = \rho\omega^2 \frac{\left(\tilde{\mathbf{K}}\nabla\mathbf{U}\right)^T \tilde{\mathbf{M}}\mathbf{U}}{\left(\tilde{\mathbf{K}}\nabla\mathbf{U}\right)^T \tilde{\mathbf{K}}\nabla\mathbf{U}}, \tag{29}$$

and assigns G to voxel $\mathbf{i}$. The same mesh of elements is used for each voxel and therefore the matrices $\tilde{\mathbf{M}}$ and $\tilde{\mathbf{K}}$ can be precomputed. The mesh recommended here is shown in Figure 1 where the center of the mesh is located at the current voxel. In the orthogonal directions the mesh contains 5 voxels and the use of tetrahedral elements allows for the approximation of a sphere of this diameter. The mesh contains 65 nodes and so, with three displacement components, this leads to 195 complex equations to solve for one complex stiffness value. 30 of the 65 nodes line up directly with voxels and those that do not use linearly interpolated displacement data.

This mesh was found to balance being large enough to construct good estimates of the moduli while being as small as possible. A small mesh is desirable for local methods as the local homogeneous assumption will more likely be valid in a greater number of voxels. An added benefit of a smaller mesh is that it leads to a smaller system size which further reduces computational time. It is assumed that during acquisition and pre-processing that reasonable data quality and voxel-to-wavelength ratio has been achieved, so that a 5-voxel diameter mesh is sensible. If this is not true then the suggested approach is to interpolate the wave data onto a finer or coarser mesh so that 5-voxel estimates are more sensible.

The element used for the local method is based on the tetrahedral $\mathbb{P}^2$-$\mathbb{P}^1$ element. The standard $\mathbb{P}^2$-$\mathbb{P}^1$ element is inf-sup stable by representing the displacements by quadratic basis functions and the pressures by linear basis functions (Hughes, 2000). In elastography, the wave data will inherently contain noise and quadratic interpolations will amplify this more than linear interpolations. For this reason, a unique element is used where the displacements are represented on smaller linear sub-elements which fit inside the larger linear elements used

ACCEPTED MANUSCRIPT

for pressure. An illustration of these elements can be seen in Figure 1. This element is expected to retain inf-sup stability as this condition has to do with the ratio of the numbers of constraints and not with the order of the approximation (Hughes, 2000). A discrete inf-sup calculation using matrices constructed from the described mesh yields $\beta_h = 8.7861 \times 10^{-4} > 0$.

Several further improvements are now described for the proposed local method. The first is to solve for the square of the wave number, k^2, instead of G, where $k^2 = \rho\omega^2/G$. The equations to solve become

$$k^2 \tilde{\mathbf{M}}\mathbf{U} = \tilde{\mathbf{K}}\nabla\mathbf{U} \tag{30}$$

and the least squares solution is

$$k^2(\mathbf{i}) = \frac{\left(\tilde{\mathbf{M}}\mathbf{U}\right)^T \tilde{\mathbf{K}}\nabla\mathbf{U}}{\left(\tilde{\mathbf{M}}\mathbf{U}\right)^T \tilde{\mathbf{M}}\mathbf{U}}. \tag{31}$$

The only difference with equation (29) is that equation (31) contains the mass type matrix, $\mathbf{M}$, in the denominator instead of the Laplacian type matrix, $\mathbf{A}$. It is hypothesized, since $\mathbf{A}$ represents the Laplacian, it will amplify the effects of noise, and therefore that replacing it with $\mathbf{M}$ in the solution will improve the reconstructed elasticity by reducing noise effects. The complex modulus is then calculated by the scalar operation $G(\mathbf{i}) = \rho\omega^2/k^2(\mathbf{i})$.

The second improvement is to remove non-physical equations from the least squares solution. As seen in (30) and (31), many equations combine via least squares to give a single value of k^2. So, any individual equation that gives a non-physical value for k^2 is removed. The equations for $\mathrm{Re}\left(k^2\right)$ and $\mathrm{Im}\left(k^2\right)$ are processed separately, so an equation for $\mathrm{Re}\left(k^2\right)$ which gives a negative value or an equation for $\mathrm{Im}\left(k^2\right)$ which gives a positive value is excluded. All remaining equations are combined via least squares minimization to solve for k^2. This procedure is expected to reduce variation and increase accuracy of G' and G'', although if the true values are near zero this procedure may introduce a bias towards larger values by removing all negative contributions. In the case that all equations give a non-physical value, then only the single equation that

ACCEPTED MANUSCRIPT

gives the closest-to-valid value is used. Due to the large number of equations given by the kernel this case is extremely rare and does not occur in any of the results presented here. Other techniques to optimize the least squares solution include total least squares (Okamoto et al., 2011) and, in work on ultrasound elastography reconstruction, interatively reweighted least squares (Rivaz et al., 2011).

Finally, a residual-based weighted average is used as a post-processing step. The residual at each voxel is calculated by

$$R(\mathbf{i}) = \|k^2(\mathbf{i})\,\tilde{\mathbf{M}}\mathbf{U} - \tilde{\mathbf{K}}\nabla\mathbf{U}\|. \tag{32}$$

In theory, voxels in which the constant stiffness assumption is more valid will have a lower residual than their surrounding voxels. Also, the finite element mesh for any one voxel includes the surrounding voxels and therefore the reconstructed G is valid, to some degree, for any of the voxels in that mesh. From these observations, the approach chosen here is to consider the $3 \times 3 \times 3$ cube centered around the current voxel and compare the residuals within that set of voxels, including the current voxel. The stiffness from any voxels in that set with residual less than or equal to the current voxel's residual will be averaged. A weighted averaging of the stiffness is performed where the weights are one over the residual, so that the new stiffness at voxel $\mathbf{i}$ is given by

$$G(\mathbf{i}) = \sum_{\substack{\mathbf{k} \\ R(\mathbf{k}) \leq R(\mathbf{i})}} \frac{G(\mathbf{k})}{R(\mathbf{k})} \;/\; \sum_{\substack{\mathbf{k} \\ R(\mathbf{k}) \leq R(\mathbf{i})}} \frac{1}{R(\mathbf{k})} \tag{33}$$

where $\mathbf{k}$ counts over the voxels in the $3 \times 3 \times 3$ cube. Voxel-wise residual error values have also been used in other MRE reconstruction work to invalidate stiffness values in certain voxels (Okamoto et al., 2011) and identify heterogeneities (Okamoto et al., 2014). Here, the post-processing step described above affects the elastogram itself, automatically replacing stiffness values in regions with high error (such as near heterogeneities) and simply smoothing the elastogram in regions of low error.

ACCEPTED MANUSCRIPT

2.6. Local curl reconstruction (revisited)

The process of voxel-wise assignment of stiffness values found from least squares solutions of Helmholtz-like equations is shared between the proposed and local curl methods. Therefore, the improvements described above are easily applied to the latter. In the interest of comparing the methods in their optimal configuration, the curl method is enhanced by solving for k^2 and by removing non-physical equations. In this case, as there are only three equations for each of the two unknowns at each pixel, it is more likely that all three are non-physical and therefore more likely that the elastograms will contain voxels with non-physical stiffness values. Optionally, these voxels could also be set to zero stiffness or be registered as invalid and removed from any subsequent steps. Finally, as a post-processing step, a Gaussian filter is applied to the elastogram itself with $3 \times 3 \times 3$ support and $\sigma = 1$ voxel.

3. Results

The reconstruction methods described in Section 2 were assessed by applying them to a range of MRE data sets. Verification of the methods, by reconstructing phantom data with known stiffness distributions, is described first. Next, several tests for investigating the methods' robustness to noise are introduced and the results of these tests are presented. Multiple anatomical data sets were considered in order to show the methods' robustness to complex data and the resulting correlation of stiffness to anatomy. Table 1 contains a summary of the phantom and anatomical data sets used in this work. The sequence used to acquire these data sets is described in (Garteiser et al., 2013). For the global method, the regularization parameters were optimized in each data set by varying the parameters over many reconstructions and comparing the results with the corresponding magnitude image. All methods were applied as described in Section 2 except that for the curl-based method a Gaussian filter was applied to the raw displacement data with $3 \times 3 \times 3$ support and $\sigma = 0.5$ voxels. This was to ensure that the proposed and curl reconstructions have equivalent spatial

ACCEPTED MANUSCRIPT

Data set	Hz	Resolution	Cropped	Voxel size
CIRS phantom	90	160×160×12	75×35×11	2×2×2 mm
Breast phantom	200	64×64×7	63×63×7	2×2×2 mm
Breast	60	160×160×12	47×47×11	2×2×2 mm
Brain*	30	64×64×12	55×55×11	3×3×3 mm

Table 1: Summary of the data sets used in this work. From left to right: the data set, acquisition sequence information, vibration frequency, original resolution of the MRE images, resolution of the cropped data used for reconstruction, and voxel size. *There are three brain data sets with the same size and information. These were taken sequentially of the same volunteer in the same sitting.

support through pre-processing, reconstruction, and post-processing steps. In order to show the tendency for the methods to reconstruct non-physical (negative) values for G'', the scales on the G'' elastograms for all data sets include negative values. Finally, the computational cost of the methods is briefly presented.

3.1. CIRS Phantom

The reconstruction methods were first applied to data from the CIRS 049 elastography phantom which is made from Zerdine material and contains four spherical inclusions of varying stiffness (CIRS Inc., Norfolk, VA, USA). While the storage modulus, G', varies between the background and the four inclusions, the loss modulus, G'', should be essentially zero throughout. The middle slice of the real x displacements and the magnitude image are shown in Figure 2 with stiffness reconstructions for the original local curl, improved local curl, global, and proposed methods. The original (Section 2.2) and improved (Section 2.6) curl methods are shown here in order to analyze the effects of the listed improvements. The five regions were segmented based on the magnitude image and stiffness means and standard deviations were calculated for the three methods over the middle three slices. These values, along with manufacturer provided values, are presented in Table 2 and plotted in Figure 3, where the region numbers refer to the areas shown in the magnitude image in Figure 2. The

ACCEPTED MANUSCRIPT

	G' (kPa)					G'' (kPa)				
Region	Reported	Curl (Orig)	Curl	Global	Proposed	Reported	Curl (Orig)	Curl	Global	Proposed
1	1.33	1.09±0.12	1.15±0.11	1.58±0.13	1.59±0.12	0	0.14±0.03	0.15±0.04	0.13±0.06	0.20±0.03
2	2.20	1.67±0.09	1.74±0.10	2.11±0.09	2.09±0.07	0	0.14±0.07	0.17±0.06	0.14±0.11	0.17±0.04
3	7.87	3.90±0.69	3.71±0.55	5.06±0.21	4.42±0.34	0	0.33±0.50	0.48±0.38	0.26±0.15	0.67±0.15
4	12.60	4.22±1.56	4.55±0.93	6.36±0.32	5.87±0.98	0	0.63±1.74	1.52±0.81	0.32±0.34	1.80±0.65
5	3.73	2.94±0.57	2.88±0.54	3.44±0.53	3.44±0.45	0	-0.01±0.38	0.29±0.24	0.16±0.19	0.31±0.18

Table 2: Reported and reconstructed values for the CIRS phantom within each of the five regions. Means and standard deviations are given for the reconstructed values.

regularization parameters for the global method were optimized to $\alpha_G = 10$, $\alpha_{P1} = 1$, and $\alpha_{P2} = 0$.

3.2. Breast Phantom

The second phantom data set, used to further verify the methods, is a breast phantom made from oil-in-gelatin dispersions (Madsen et al., 2006). This phantom is divided into two background areas and two inclusions meant to model breast tissue and tumours. The regions mimic subcutaneous fat (S), glandular tissue (G), cancer (C), and fibroadenoma (F). In contrast to the CIRS phantom, both the storage and loss moduli vary between the four areas. The middle slice of real z displacements, magnitude, and stiffness reconstructions for the three methods are shown in Figure 4. Again, the regions are segmented according to the magnitude image and stiffness means and standard deviations are calculated over the middle slice. These values are compared with measured values of the phantom in Table 3 and Figure 5. The measured values are taken from (Sinkus et al., 2007) where a multifrequency analysis was performed which incorporated the rheometer measured values from (Madsen et al., 2006). The ranges provided in (Sinkus et al., 2007) are incorporated into the error bars here. Regularization parameters for the global method were optimized to $\alpha_G = 10^{3.5}$, $\alpha_{P1} = 1$, and $\alpha_{P2} = 0$.

ACCEPTED MANUSCRIPT

	G' (kPa)					G'' (kPa)				
Region	Measured	Curl (Orig)	Curl	Global	Proposed	Measured	Curl (Orig)	Curl	Global	Proposed
S	5.90±1.00	5.35±1.06	5.54±0.84	6.78±1.12	7.84±0.79	1.19±0.81	0.22±0.65	0.62±0.43	0.24±0.51	0.77±0.39
G	12.50±2.40	10.27±1.33	10.38±1.17	10.93±1.16	11.89±0.75	1.20±0.50	0.23±0.78	0.89±0.54	0.20±0.62	0.84±0.42
C	21.95±4.55	13.49±2.12	13.19±1.25	14.33±1.33	15.00±1.06	1.85±0.95	1.88±1.29	2.86±0.79	0.16±0.42	1.93±0.53
F	31.90±3.05	12.79±3.53	13.99±2.66	15.93±2.08	15.36±2.05	2.30±1.10	-2.37±1.94	2.10±1.74	1.01±0.54	1.97±0.54

Table 3: Rheometer measured and reconstructed values for the breast tissue phantom in each of the four regions. Means and standard deviations are given for reconstructed values. The mean and error for the measured values are taken from (Sinkus et al., 2007).

3.3. Robustness to noise

Several tests were developed and run to determine the robustness of each reconstruction method to noise in the displacement data. Effects of both the true noise, inherent in the image, and artificially added noise were tested. These tests were applied to both the CIRS phantom and breast phantom data sets, with results summarized in Figures 6 and 7, respectively. A total of six tests were considered:

- %Er - Percent error between the mean reconstructed G' value and the reported or measured value,
- SD G' , SD G'' - The standard deviation of reconstructed G', G'',
- %Dec - The percent decrease in the mean reconstructed G' when 6% noise is added,
- MSD G' , MSD G'' - Mean standard deviation of G' , G'' over 50 cases with 6% random noise added to each.

The %Er, SD, and %Dec tests consider stiffness values from region 5 in the CIRS phantom and region G in the breast phantom. The two MSD tests consider values from the entire data set. For all tests, data from the middle five slices of the CIRS phantom and the middle three slices of the breast phantom were used.

ACCEPTED MANUSCRIPT

While the %Er metric could be presented as a test of accuracy it is used here to measure robustness to noise. It is presumed that, for direct methods, the SNR and the ratio of wavelength to voxel size define a stiffness threshold where higher stiffness values will be underestimated and lower values will be overestimated (Arunachalam et al., 2017; Connesson et al., 2015; Honarvar et al., 2016; Papazoglou et al., 2008). This can be seen in Figures 3 and 5 as well as in phantom results presented in other work (Baghani et al., 2011; Honarvar et al., 2012, 2013). For typical MRE data quality, this ideal wavelength to voxel size ratio has usually been found to lie approximately between 10 and 20 Arunachalam et al. (2017); Honarvar et al. (2016). Since all three methods underestimate G' in region 5 of the CIRS phantom and region G of the breast phantom, it is assumed that these values lie above this threshold in their respective data sets. Furthermore, stiffness values should decrease when high frequency noise is added, as higher frequencies correspond to lower stiffness values. Therefore, the less affected the method is by noise, the more accurate these average values of G' will be.

The SD metrics assess the variability of the stiffness results, in what should be homogeneous regions of the phantoms, by computing the standard deviations of G' and G'' within those regions. The %Dec metric measures the percent decrease in the mean G' value with approximately 6% uniformly distributed random noise added to every component of the displacement field. The final two tests, denoted as MSD for *mean standard deviation*, measure the precision of the methods in the presence of increased noise. The phantom data sets were reconstructed 50 times, where, for each reconstruction, 6% random noise was added (as for %Dec). The standard deviation of the 50 stiffness values computed for each pixel was calculated and scaled by the mean of the 50 values. The final value for this test is then the mean over the entire data set of these scaled standard deviations, so that a lower value indicates a higher precision reconstruction. If the mean at a pixel was less than 10 Pa, then that data was removed to avoid dividing by small numbers.

For all six tests a low value is desirable. To construct the spider plots (Figures

ACCEPTED MANUSCRIPT

6 and 7) the raw numbers from each test are inverted and then scaled by the maximum inverted value for that test. So the best performing method has a value of 1 and appears on the outer rim of the plot, with the center of the plot corresponding to 0. The global methods were run with the same regularization parameters as specified for the verification results.

3.4. In vivo data

To evaluate the performance of the reconstruction techniques in vivo, the methods were applied to healthy volunteer breast and brain data sets. For the breast data, the middle slices of reconstructed G' and G'' are shown in Figure 8 along with the real x displacements and the magnitude image. In order to investigate the effects of the pressure regularization, the global method was run with two different sets of parameters. The first result used $\alpha_G = 10^3$, $\alpha_{P1} = 10^2$, and $\alpha_{P2} = 10^1$ and the second result used $\alpha_G = 10^3$, $\alpha_{P1} = 10^0$, and $\alpha_{P2} = 10^1$.

The reconstruction methods were also applied to three data sets of human brain data. These data sets were taken sequentially of the same volunteer in the same sitting. The middle slices of G' and G'' are shown in Figure 9 aside magnitude images. The global method had regularization parameters optimized to $\alpha_G = 10^4$, $\alpha_{P1} = 10^5$, and $\alpha_{P2} = 10^5$, which were chosen based on the second data set, as this appeared to give reasonable values for G' and correlation to anatomy. These parameters were then applied to the other two data sets. Symmetry measures for each method were computed by flipping the elastograms over the line of symmetry, subtracting from the originals, and taking the two-norm of the difference so that a lower number means more symmetry. G' and G'' values were averaged over the three data sets. The proposed method gives 10.4 and 7.8 for G' and G'' symmetry, respectively. The curl method gives 11.6 and 8.5 and the global method gives 11.5 and 10.3.

Additional information is provided in Figure 10 in order to better contextualize the brain results. This figure shows, for each of the three data sets, the wave amplitude, $\sqrt{|u_x|^2 + |u_y|^2 + |u_z|^2}$, and the percentage contribution from upper

ACCEPTED MANUSCRIPT

Data set	Total # of voxels	Reconstruction time (seconds)			
		Curl (Orig)	Curl	Global	Proposed
CIRS phantom	28,875	3.4	3.6	73.5	9.3
Breast phantom	27,783	3.1	3.2	62.4	7.3
Breast	24,299	2.8	2.9	49.3	6.7
Brain	33,275	5.0	5.2	87.9	9.8

Table 4: Time to complete reconstructions for the local curl, global, and proposed methods in seconds. Times are averages of 3 runs. The small difference between the original and improved curl methods is due to the relatively large amount of time spent on the pre-computation of displacement derivatives.

harmonics, which is an approximate measure of data quality. Values for this measure below 10% are typically considered to be very good, and values above 25% are considered undesirable. Also shown, are percent differences between the amplitudes for each pair of data sets.

3.5. Computational cost

The computational cost of the methods is presented in Table 4 and includes the pre-computation of displacement derivatives. The methods were applied to each data set 3 times and the average run time was calculated. The total number of voxels refers to the cropped image stack resolution as shown in Table 1. All reconstructions were run on a Linux workstation using MATLAB with an Intel Xeon 4-core (8-thread) 3.60 GHz processor.

4. Discussion

4.1. Verification

The local curl, global FEM, and proposed methods were verified by performing reconstructions on two phantom data sets. The CIRS phantom contains four inclusions with varying G' and zero G'' throughout. As seen in Figure 2, all three reconstruction methods give G' elastograms that are consistent with the magnitude image. The quality of these is such that inclusions can be identified

ACCEPTED MANUSCRIPT

and at least qualitative conclusions regarding the phantom's stiffness distribution can be reached. Here, the positive effects of the improvements can also be seen by comparing the original and improved curl methods. Even the improved curl method shows what is typical behavior of many local direct methods at the inclusion boundaries, which is to under- and overestimate stiffness on either side of large discontinuities. This is due, in part, to the invalidity of the homogeneity assumption in that region. In contrast, the proposed method provides more accuracy near inclusion boundaries, approaching that of the global method, mostly due to the residual-based weighted averaging technique and the small support. The global method provides the most accurate reconstruction for this data. All inclusions are well-defined and the G'' elastogram predicts near zero values throughout.

Both local methods predict large values for G'' in the hardest inclusion, which is probably due, in part, to the large discontinuity at this boundary, as the invalidity of the homogeneity assumption will lead to fluctuations in both components of G. Additionally, since the effects of noise are greater for longer wavelengths, as in the hardest inclusion, the variability of G will be highest in the inclusion. Removing invalid equations in the curl and proposed methods will then lead to an overall increase in G''. More generally, a limitation of the equation removal approach is that increasing noise will lead to increasing G'' in any material with zero or very low G''. However, this approach works to increase robustness and decrease variability of both G' and G'' and typically tissue (unlike phantom material) does not have a near zero G'' component.

The average stiffness values in each region of the phantom are summarized in Figure 3 and Table 2 where all methods are seen to give accurate values for the background and two soft inclusions. The large discrepancies in the harder inclusions have been explained in other publications by deterioration of the phantom or temperature during the MRE scan. It is assumed here however that this is due to the ratio of wavelength to voxel size being far from the ideal ratio as described in Section 3 and in previous work (Arunachalam et al., 2017; Honarvar et al., 2016; Papazoglou et al., 2008).

ACCEPTED MANUSCRIPT

The breast phantom (elastograms shown in Figure 4) has a more significant G'' component with known values and distribution, potentially making this data more difficult to reconstruct. The G' elastograms from all three methods give comparable accuracy to the CIRS phantom data. Here, however, the ratio between the inclusion stiffness and background stiffness is lower which reduces the ringing effect for the curl method and presumably the variability in G'' near the inclusions for both local methods. In the G'' elastograms the inclusions are not clearly identifiable in the global method reconstruction but are for both local method reconstructions. In Figure 5 and Table 3, the proposed method is shown to accurately predict the mean G'' for all regions.

Overall, considering both phantom data sets, the proposed method is seen to approach the accuracy of the more expensive global method for G'. It also shows higher accuracy and lower variability than the curl method, in addition to reducing negative effects of the local homogeneity assumption. In Tables 2 and 3 a general increase in accuracy and decrease in variance between the original and improved curl methods shows the benefit of some of the proposed improvements. The accuracy of the averages in Tables 2 and 3 and Figures 3 and 5 is comparable between the proposed and global methods, while the curl method is slightly less accurate overall. While results for G'' are generally more variable, the proposed method is able to provide a meaningful and physically valid G'' distribution in the breast phantom.

4.2. Sensitivity

The sensitivity analysis performed here quantifies the effects of noise on the reconstruction methods in order to determine robustness. This analysis consisted of six tests and is summarized in the spider plots in Figures 6 and 7, corresponding to the CIRS phantom and breast phantom data, respectively. The %Er and %Dec tests consider changes in mean values of stiffness, as high frequency noise will tend to lower the reconstructed stiffness, while the SD G', SD G'', MSD G', and MSD G'' tests consider the standard deviation of reconstructed stiffness. These latter four tests are directly affected by the degree of

ACCEPTED MANUSCRIPT

averaging and regularization within the three methods (i.e. any standard deviation result could be achieved by adjusting the averaging or regularization). Therefore, it is necessary to consider the detail in the elastograms themselves. As the elastograms for both phantoms show similar definition of region boundaries and the local methods have equivalent spatial support, the standard deviation tests are assumed to be a valid comparison.

The %Er and %Dec tests consider mean G' values over the phantom background areas, specifically the discrepancy from the true value and the decrease when artificial noise is added to the displacements, respectively. In these tests, the proposed method appears to be more robust than either the curl or global method in both phantoms. It reconstructs both a higher average stiffness with only the inherent noise in the original data and is less affected by additional noise.

The proposed and curl methods perform better than the global method in the MSD G'' test, probably due to the removal of non-physical equations. The G'' reconstruction is more sensitive, and G'' is closer to zero, so presumably additional noise increases the likelihood of these equations becoming non-physical. Therefore removing those non-physical equations reduces the deviation of the result but, as described previously, will result in an artificial increase in the reported value. The MSD G' test shows the proposed method performing slightly better than the global method in both phantoms. While the former two tests consider variability due to added artificial noise, the SD G' and SD G'' tests consider variability due to causes within the original data, including any inherent noise. In this case, the proposed method again shows less variability for both components of G and the global and curl methods show similar results.

The MSD G' test is also used to show the relation between precision and SNR in Figure 11 for the proposed method while using the CIRS phantom data. MSD G' values were computed over different noise levels and the results are plotted against the average wave amplitude divided by the amplitude of the added noise, A_w/A_n. So, the unaltered waves, although including some amount of inherent noise, are assumed for this result to have infinite SNR. For example,

ACCEPTED MANUSCRIPT

the 6% noise used in the original MSD G' test, or $A_w/A_n \approx 16$, leads to an MSD value of about 4%.

Finally, the proposed method seems to be relatively more robust in the breast phantom than in the CIRS phantom compared to the global method. This may be due to the breast phantom being more complicated because of the significant G'' component. Overall, these tests show that the proposed method generally performs better than the global method which in turn performs better than the curl method.

4.3. In vivo

To evaluate reconstruction performance on real data, both breast and brain data sets were considered.

4.3.1. In vivo breast data

The reconstructed elastograms in Figure 8 show that the stiffer glandular region is identifiable in G' for all three methods as well as in G'' for the proposed and curl methods. Both the curl and global methods predict G'' to have non-physical (negative) values in some regions. Although the curl method removes non-physical equations, some of the voxels for this data set give all non-physical equations for G''. In contrast, the proposed method predicts only positive values throughout. All three methods give qualitatively reasonable results and similar ranges for G', including both instantiations of the global method. The proposed method gives an average stiffness of 1.62 kPa in the glandular region and 0.79 kPa in the subcutaneous fat while the curl method averages 1.07 and 0.47 kPa and the global method averages 2.11 and 0.83 kPa in these respective regions. The other choice of pressure regularization for the global method gives 1.81 and 0.79 kPa in these regions. These values are near or within previously reported ranges (Samani et al., 2007; Sinkus et al., 2005b), and the lower values for the curl method may be due to noise sensitivity. The stiffness distributions themselves also differ, as the global method shows a single large area of increased stiffness while the proposed and curl methods show a more constant

ACCEPTED MANUSCRIPT

baseline stiffness with several localized areas of increased stiffness. The breast data was also used to demonstrate the effect of the global method's pressure regularization on reconstructed stiffness. It was found that adjusting the pressure regularization in this data set could result in local changes in G' of up to about 1 kPa (45%), and in the average glandular values by about 15%.

4.3.2. In vivo brain data

Brain potentially represents a more challenging arena for MRE reconstruction as there is a greater likelihood of anisotropic tissue and because the brain contains areas, such as the ventricles, that do not conform to linear elastic assumptions. On the other hand, because the brain is symmetric between left and right hemispheres, it offers a way to validate the reconstruction as stiffness is expected to follow this symmetry. The brain data presented here also offers a way to judge the reproducibility of the reconstructions because the three data sets were taken sequentially of the same volunteer in the same sitting, and therefore the elastograms should be similar.

The local curl method, as with the other data sets, gives lower values for G' with more variability. It does, however, show correlation to anatomy, including some symmetry in both stiffness moduli. The proposed method's elastograms also correlate well with anatomy and show symmetry across much of G'' and some areas of G'. These show less variability than the curl results and physically meaningful values throughout. According to the symmetry measures (Section 3.4), the proposed method shows slightly improved symmetry in both stiffness components over the comparison methods. In contrast, the global method shows little correlation with anatomy as the results contain local patches of high and low stiffness in both G' and G'' that are not symmetric and presumably not physically reasonable. There also seems to be less detail in the global method's elastograms than in the local methods'. In general, this could be caused by too large of a stiffness regularization parameter, however, the faint checkerboard pattern indicates that, if anything, the stiffness regularization is probably slightly too low.

ACCEPTED MANUSCRIPT

The proposed and curl methods seem to show reproducibility judging by the similarity between the scans. Even the second scan, which has overall lower values for the moduli, shows similar stiffness distributions for both methods. In contrast, the global method shows inconsistent results for both moduli. The regularization parameters were selected considering only the second scan and based on seeing some degree of symmetry and reasonable values throughout the domain. While the G'' image for the second scan does not seem to correlate to anatomy, the G' image appears reasonable. Applying these parameters directly to the other two scans, which should be very similar, leads to inconsistent results that do not correlate with the magnitude images.

To better contextualize the brain results, additional information has been provided in Figure 10. It is shown that differences in the waves between scans lead to changes in wave amplitude of nearly 8% across various regions. Furthermore, the contribution from upper harmonics (an indication of data quality) is not symmetric for these data and is not identical between scans. It is therefore unlikely that direct reconstruction methods, which depend strongly on data quality, would provide perfectly symmetric and consistent stiffness distributions for this particular set of data. Considering this, direct methods that are less sensitive to data quality should show more symmetry, as the proposed method does.

4.4. Clinical applicability

The *in vivo* data sets presented here are meant to be representative, in terms of resolution and quality, of typical data that may be collected by clinical MRE users. Brain MRE is still developing and many data sets in the literature show more symmetry than those presented here, and hence are presumably of greater quality. This is purposeful however, as an interest here is robustness of methods to varying data quality and, as described above, some lack of symmetry allows for better separation of the methods. Since the image resolutions are comparable to clinical resolutions, the compute times presented in Table 4 are applicable to proposed clinical time lines. As shown, the global method takes almost an

ACCEPTED MANUSCRIPT

order of magnitude more time to reconstruct than the local methods. While compute times of around one minute may not be prohibitive, the global method also requires multiple runs in order to optimize the regularization parameters. The local methods, in contrast, are fast and easy-to-use (being parameter-less). Parameter adjustment may be necessary during pre-processing steps, such as smoothing and unwrapping, but this is the case for all methods, and also, some prior knowledge or know-how may be necessary to ensure reasonable data quality and voxel to wavelength ratio. Ease-of-use, in addition to low computational expense, could allow for a very quick turnaround during clinical scans, perhaps indicating that collection of higher quality data is required before removing a patient from the MRI. Additionally, potential modifications to preprocessing could be more quickly tested.

The global method does not assume local stiffness homogeneity, allowing this method to more correctly model the underlying physics. Unfortunately, this causes instability in the method which requires regularization of both the stiffness and pressure. The stiffness regularization parameter, α_G, is straightforward to optimize: too low and the result will resemble a checkerboard pattern, too high and the elastogram will be blurred with loss of definition. However, as shown here (Figure 8), the pressure regularization parameter, α_{P1}, can significantly affect the stiffness and require optimization to perfect the result. Even within one type of scan, as in Figure 9, one set of parameters may not work for each data set. This could be due to differences in SNR or small changes in wave behavior affecting the stability of the method. Properly regularizing the pressure may become more difficult as the significance of the pressure component increases (as it does in these studies from phantoms to breast to brain). For example, a very specific set of parameters may be required or the parameters may need to vary spatially. Increasing pressure regularization may also require a rebalancing of the stiffness regularization to maintain similar definition in the elastogram.

Problematic data may pollute global methods whereas these problems are localized in local methods. Therefore, global methods may require careful mask-

ACCEPTED MANUSCRIPT

ing of certain regions or problematic data (this would be more complicated than the removal of non-physical equations in the proposed method). These regions or data could also require increased regularization to further constrain the solution or lead to more difficulty in finding optimized parameters. This may be occurring in these data sets, as deviations from isotropic linear elastic assumption become more probable from phantoms to breast to brain. While global methods have the potential to produce more accurate stiffness reconstructions, more work is required for this class of methods to be quickly applicable to a range of data sets while giving robust, consistent, and accurate results.

More data may reduce the negative influences of the issues discussed above. Additional data could come from multiple scans, either utilizing different transducer locations or frequencies. So called multifrequency reconstructions have been successful but require correct handling of the frequency dependence of stiffness and, of course, longer scan times (Honarvar et al., 2013; Papazoglou et al., 2012; Tzschätzsch et al., 2016). While this would improve the results of the global method, potentially helping to stabilize the solution, it would also improve results for the curl and proposed methods. As iterative methods become more ubiquitous, standardized, and tractable these too may find more use in clinically oriented work as they are potentially less biased by data quality.

The proposed div-free FEM method shares the underlying assumption of local homogeneity with the curl method. This assumption leads to inaccuracies in some portions of the elastogram, however, it allows for stable, parameter-less, and fast reconstructions. Through utilizing residual-based weighted averaging and a small support, the proposed method is able to mitigate the drawbacks of this assumption. It uses additional features to reduce noise sensitivity allowing it to reconstruct different types of in vivo data in a consistent and robust manner.

5. Conclusion

The local direct div-free FEM method for MR elastography reconstruction was shown to accurately and robustly reconstruct stiffness in both phantom and

ACCEPTED MANUSCRIPT

in vivo data. The FEM as well as polynomial fitting for derivative calculations have been shown in prior work to increase robustness and so were utilized here. Further advancements were presented which increase accuracy, reduce noise sensitivity, and mitigate the drawbacks of the local homogeneity assumption. These improvements include adjustments within the FEM, such as a unique linear inf-sup stable element to achieve a low order approximation of the noisy displacements but maintain correct inf-sup stability for the mixed pressure-displacement form of the equations. Divergence-free test functions eliminate the compressional term, reduce the system size, and simplify the equations. A tetrahedral mesh with small support limits the inaccuracies caused by the local homogeneity assumption while providing many constraints per unknown. Other techniques include solving for k^2, removing non-physical equations, and residual-based weighted averaging which all contribute towards increased accuracy and reduced sensitivity.

Comparisons were made between the proposed div-free FEM method and two state-of-the-art reconstruction methods: a local curl-based approach and a global heterogeneous approach. The proposed and curl-based approaches are easily and quickly applied to data as they are fast and parameter-less, although the proposed method showed increased accuracy and reduced sensitivity in comparison. In phantoms, the proposed method had comparable accuracy to the more expensive and parameter-dependent global method, but again, showed reduced sensitivity to noise. In anatomical data, results from the global method showed a strong dependence on parameters in breast data and a lack of consistency over brain data sets, whereas the proposed method showed consistency and correlation to anatomy.

Acknowledgments

This research is funded by the European Union's Horizon 2020 Research and Innovation Programme under grant agreement No 668039 and by the European Research Council under the European Union's Seventh Framework Programme

ACCEPTED MANUSCRIPT

(FP/2007-2013)/ERC Grants Agreement No. 600948. The authors would like to acknowledge funding from Engineering and Physical Sciences Research Council (EP/N011554/1).

Appendix A. Finite element matrix construction

The FEM system for the global method (equation 23) contains matrices $\mathbf{M}$, $\mathbf{C}$, and $\mathbf{K}$. The mass matrix, $\mathbf{M}$, is given by

$$\mathbf{M} = \begin{pmatrix} \mathbb{M} & 0 & 0 \\ 0 & \mathbb{M} & 0 \\ 0 & 0 & \mathbb{M} \end{pmatrix} \tag{A.1}$$

and

$$\mathbb{M}_{ij} = \int_\Omega \psi_i^u \psi_j^u \, \mathrm{d}\Omega, \tag{A.2}$$

where $i = 1, ..., N_w$ and $j = 1, ..., N_u$. So, i and j count over the nodes representing $\mathbf{w}$ and $\mathbf{u}$, respectively. Likewise, $\mathbf{C}$ is given by

$$\mathbf{C} = \begin{pmatrix} \mathbb{C}_1 & \mathbb{C}_2 & \mathbb{C}_3 \end{pmatrix}^T \tag{A.3}$$

and

$$(\mathbb{C}_k)_{ij} = \int_\Omega \psi_j^p \frac{\partial \psi_i^u}{\partial x_k} \, \mathrm{d}\Omega, \tag{A.4}$$

where $i = 1, ..., N_w$ and $j = 1, ..., N_p$. Finally, $\mathbf{K}$, which contains precomputed derivatives of the measured displacements, is given by

$$K_{ij} = \begin{pmatrix} \mathbb{K}_{1ij} & \mathbb{K}_{2ij} & \mathbb{K}_{3ij} \end{pmatrix}^T \tag{A.5}$$

and

$$\mathbb{K}_{kij} = \int_\Omega \psi_j^G D\mathbf{u}^h : (\nabla \psi_i^u \otimes \hat{e}_k) \, \mathrm{d}\Omega, \tag{A.6}$$

where $i = 1, ..., N_w$, $j = 1, ..., N_G$, and $D\mathbf{u}^h$ contains summations defined by (21) and (22).

The FEM system for the proposed method (equation 28) also requires the construction of matrices $\mathbf{M}$, $\mathbf{C}$, and $\mathbf{K}$. The matrices $\mathbf{M}$ and $\mathbf{C}$ are constructed

ACCEPTED MANUSCRIPT

in the same way as above except that the integration is done over the local domain and therefore, the mesh, and hence the number of nodes, is much smaller. However, $\mathbf{K}$ is slightly different. After multiplying by $\nabla\mathbf{U}$ as described in section 2.5, the vector $\mathbf{K}\nabla\mathbf{U}$ can be represented similarly to (A.5) and (A.6) except that G is constant, so is not represented by basis functions, and the symmetric portion of the strain tensor has been removed.

References

References

Arunachalam, S. P., Rossman, P. J., Arani, A., Lake, D. S., Glaser, K. J., Trzasko, J. D., Manduca, A., McGee, K. P., Ehman, R. L., Araoz, P. A., 2017. Quantitative 3d magnetic resonance elastography: Comparison with dynamic mechanical analysis. Magn. Reson. Med. 77 (3), 1184–1192.

Baghani, A., Salcudean, S., Honarvar, M., Sahebjavaher, R. S., Rohling, R., Sinkus, R., 2011. Travelling wave expansion: A model fitting approach to the inverse problem of elasticity reconstruction. IEEE Transactions on Medical Imaging 30 (8), 1555–1565.

Bataller, R., Brenner, D., 2005. Liver fibrosis. J. Clin. Invest. 115, 209–218.

Bercoff, J., Chaffai, S., Tanter, M., Sandrin, L., Catheline, S., Fink, M., Gennisson, J. L., Meunier, M., 2003. In vivo breast tumor detection using transient elastography. Ultrasound Med. Biol. 29 (10), 1387–1396.

Bonekamp, S., Kamel, I., Solga, S., Clark, J., 2009. Can imaging modalities diagnose and stage hepatic fibrosis and cirrhosis accurately? Journal of Hepatology 50, 17–35.

Connesson, N., Clayton, E., Bayly, P., Pierron, F., 2015. Extension of the optimised virtual fields method to estimate viscoelastic material parameters from 3d dynamic displacement fields. Strain 51 (2), 110–134.

ACCEPTED MANUSCRIPT

Eskandari, H., Salcudean, S. E., Rohling, R., Bell, I., 2011. Real-time solution of the finite element inverse problem of viscoelasticity. Inverse Problems 27 (8), 085002.

Eskandari, H., Salcudean, S. E., Rohling, R., Ohayon, J., 2008. Viscoelastic characterization of soft tissue from dynamic finite element models. Phys. Med. Biol. 53, 6569–6590.

Garteiser, P., Doblas, S., Daire, J.-L., Wagner, M., Leitao, H., Vilgrain, V., Sinkus, R., Van Beers, B. E., 2012. MR elastography of liver tumours: value of viscoelastic properties for tumour characterisation. Eur. Radiol. 22 (10), 2169–2177.

Garteiser, P., Sahebjavaher, R. S., Ter Beek, L. C., Salcudean, S., Vilgrain, V., Van Beers, B. E., Sinkus, R., 2013. Rapid acquisition of multifrequency, multislice and multidirectional mr elastography data with a fractionally encoded gradient echo sequence. NMR in Biomedicine 26 (10), 1326–1335.

Glaser, K. J., Manduca, A., Ehman, R. L., 2012. Review of mr elastography applications and recent developments. Journal of Magnetic Resonance Imaging 36 (4), 757–774.

Green, M. A., Bilston, L. E., Sinkus, R., 2008. In vivo brain viscoelastic properties measured by magnetic resonance elastography. NMR in Biomedicine 21 (7), 755–764.

Guo, Z., You, S., Wan, X., Biani, N., 2010. A FEM-based direct method for material reconstruction inverse problem in soft tissue elastography. Computers and Structures 88, 1459–1468.

Honarvar, M., Rohling, R., Salcudean, S. E., 2016. A comparison of direct and iterative finite element inversion techniques in dynamic elastography. Physics in Medicine and Biology 61, 3026–3048.

Honarvar, M., Sahebjavaher, R., Sinkus, R., Rohling, R., Salcudean, S. E., 2013. Curl-based finite element reconstruction of the shear modulus without assum-

ACCEPTED MANUSCRIPT

ing local homogeneity: Time harmonic case. IEEE Transactions on Medical Imaging 32 (12), 2189–2199.

Honarvar, M., Sahebjavaher, R. S., Salcudean, S. E., Rohling, R., 2012. Sparsity regularization in dynamic elastography. Phys. Med. Biol. 57, 5909–5927.

Hughes, T. J., 2000. The Finite Element Method. Dover Publications, Inc., Mineola, New York.

Huwart, L., Sempoux, C., Vicaut, E., Salameh, N., , Annet, L., Danse, E., Peeters, F., Ter Beek, L. C., Rahier, J., Sinkus, R., Horsmans, Y., Van Beers, B. E., 2008. Magnetic resonance elastography for the noninvasive staging of liver fibrosis. Gastroenterology 135 (1), 32–40.

Jamin, Y., Boult, J. K. R., Li, J., Popov, S., Garteiser, P., Ulloa, J. L., Cummings, C., Box, G., Eccles, S. A., Jones, C., Waterton, J. C., Bamber, J. C., Sinkus, R., Robinson, S. P., 2015. Exploring the biomechanical properties of brain malignancies and their pathologic determinants in vivo with magnetic resonance elastography. Cancer Research 75 (7), 1216–1224.

Kemper, J., Sinkus, R., Lorenzen, J., Nolte-Ernsting, C., Stork, A., Adam, G., 2004. MR elastography of the prostate: Initial in-vivo application. Rofo-fortschritte Auf Dem Gebiet Der Rontgenstrahlen Und Der Bildgebenden Verfahren 176 (8), 1094–1099.

Kolipaka, A., Araoz, P. A., McGee, K. P., Manduca, A., Ehman, R. L., 2010. Magnetic resonance elastography as a method for the assessment of effective myocardial stiffness throughout the cardiac cycle. Magn. Reson. Med. 64, 862–870.

Krouskop, T. A., Wheeler, T. M., Kallel, F., Garra, B. S., Timothy, H., 1998. Elastic moduli of breast and prostate tissues under compression. Ultrasonic Imaging 20, 260–274.

ACCEPTED MANUSCRIPT

Kruse, S. A., Rose, G. H., Glaser, K. J., Manduca, A., Felmlee, J. P., Jr., C. R. J., Ehman, R. L., 2008. Magnetic resonance elastography of the brain. NeuroImage 39, 231–237.

Li, S., , Chen, M., Wang, W., Zhao, W., Wang, J., Zhao, X., Zhou, C., 2011. A feasibility study of MR elastography in the diagnosis of prostate cancer at 3.0T. Acta Radiologica 52, 354–358.

Madsen, E. L., Hobson, M. A., Frank, G. R., Shi, H., Jiang, J., Hall, T. J., Varghese, T., Doyley, M. M., Weaver, J. B., 2006. Anthropomorphic breast phantoms for testing elastography systems. Ultrasound Med. Biol. 32 (6), 857–874.

Manduca, A., Lake, D. S., Kruse, S. A., Ehman, R. L., 2003. Spatio-temporal directional filtering for improved inversion of MR elastography images. Med. Image Anal. 7, 465–473.

Manduca, A., Oliphant, T. E., Dresner, M., Mahowald, J., Kruse, S. A., Amromin, E., Felmlee, J. P., Greenleaf, J. F., Ehman, R. L., 2001. Magnetic resonance elastography: non-invasive mapping of tissue elasticity. Med. Image Anal. 5 (4), 237–254.

Mariappan, Y. K., Glaser, K. J., Ehman, R. L., 2010. Magnetic resonance elastography: A review. Clin. Anat. 23, 497–511.

McKnight, A. L., Kugel, J. L., Rossman, P. J., Manduca, A., Hartmann, L. C., Ehman, R. L., 2002. MR elastography of breast cancer: Preliminary results. American Journal of Roentgenology 178 (6), 1411–1417.

McLaughlin, J., Renzi, D., Yoon, J. R., Ehman, R. L., Manduca, A., 2006. Variance controlled shear stiffness images for MRE data. IEEE Int. Symp. on Biomedical Imaging: Macro to Nano, 960–963.

Miga, M. I., 2003. A new approach to elastography using mutual information and finite elements. Physics in medicine and biology 48, 467–480.

ACCEPTED MANUSCRIPT

Murphy, M. C., Huston, John Jack, C. R., Glaser, K. J., Manduca, A., Felmlee, J. P., Ehman, R. L., 2011. Decreased brain stiffness in alzheimer's disease determined by magnetic resonance elastography. Journal of Magnetic Resonance Imaging 34, 494–498.

Oberai, A. A., Gokhale, N. H., Feijóo, G. R., 2003. Solution of inverse problems in elasticity imaging using the adjoint method. Inverse Problems 19, 297–313.

Okamoto, R., Clayton, E., Bayly, P., 2011. Viscoelastic properties of soft gels: comparison of magnetic resonance elastography and dynamic shear testing in the shear wave regime. Phys. Med. Biol. 56 (19), 6379.

Okamoto, R. J., Johnson, C. L., Feng, Y., Georgiadis, J. G., Bayly, P. V., 2014. MRE detection of heterogeneity using quantitative measures of residual error and uncertainty. In: SPIE Medical Imaging. International Society for Optics and Photonics, pp. 90381E–90381E.

Oliphant, T. E., Manduca, A., Ehman, R. L., Greenleaf, J. F., 2001. Complex-valued stiffness reconstruction for magnetic resonance elastography by algebraic inversion of the differential equation. Magn. Reson. Med. 45, 299–310.

Papazoglou, S., Hamhaber, U., Braun, J., Sack, I., 2008. Algebraic helmholtz inversion in planar magnetic resonance elastography. Phys. Med. Biol. 53 (12), 3147.

Papazoglou, S., Hirsch, S., Braun, J., Sack, I., 2012. Multifrequency inversion in magnetic resonance elastography. Physics in medicine and biology 57, 2329–2346.

Park, E., Maniatty, A. M., 2006. Shear modulus reconstruction in dynamic elastography: time harmonic case. Phys. Med. Biol. 51, 3697–3721.

Park, E., Maniatty, A. M., 2009. Finite element formulation for shear modulus reconstruction in transient elastography. Inverse Problems in Science and Engineering 17 (5), 605–626.

ACCEPTED MANUSCRIPT

Parker, K. J., Doyley, M. M., Rubens, D. J., 2011. Imaging the elastic properties of tissue: the 20 year perspective. Phys. Med. Biol. 56, R1–R29.

Paszek, M. J., Zahir, N., Johnson, K. R., Lakins, J. N., Rozenberg, G. I., Gefen, A., Reinhart-King, C. A., Margulies, S. S., Dembo, M., Boettiger, D., Hammer, D. A., Weaver, V. M., 2005. Tensional homeostasis and the malignant phenotype. Cancer Cell 8, 241–254.

Rivaz, H., Boctor, E. M., Choti, M. A., Hager, G. D., 2011. Real-time regularized ultrasound elastography. IEEE transactions on medical imaging 30 (4), 928–945.

Romano, A. J., Shirron, J. J., Bucaro, J. A., 1998. On the noninvasive determination of material parameters from a knowledge of elastic displacements theory and numerical simulation. IEEE Trans. Ultrason. Ferroelectr. Freq. Control 45 (3), 751–759.

Rouvière, O., Dresner, M. A., Rossman, P. J., Burgart, L. J., Fidler, J. L., Ehman, R. L., 2006. MR elastography of the liver: Preliminary results. Radiology 240 (2), 440–8.

Runge, J. H., Bohte, A. E., Verheij, J., Terpstra, V., Nederveen, A. J., van Nieuwkerk, K. M., de Knegt, R. J., Baak, B. C., Jansen, P. L., Sinkus, R., et al., 2014. Comparison of interobserver agreement of magnetic resonance elastography with histopathological staging of liver fibrosis. Abdominal imaging 39 (2), 283–290.

Sack, I., Beierbach, B., Hamhaber, U., Klatt, D., Braun, J., 2007. Non-invasive measurement of brain viscoelasticity using magnetic resonance elastography. NMR Biomed. 21 (4), 265–271.

Sack, I., Rump, J., Elgeti, T., Samani, A., Braun, J., 2009. MR elastography of the human heart: Noninvasive assessment of myocardial elasticity changes by shear wave amplitude variations. Magn. Reson. Med. 61, 668–677.

ACCEPTED MANUSCRIPT

Sahebjavaher, R. S., Baghani, A., Honarvar, M., Sinkus, R., Salcudean, S. E., 2013. Transperineal prostate MR elastography: Initial in vivo results. Magn. Reson. Med. 69, 411–420.

Sahebjavaher, R. S., Frew, S., Bylinskii, A., Beek, L., Garteiser, P., Honarvar, M., Sinkus, R., Salcudean, S., 2014. Prostate MR elastography with transperineal electromagnetic actuation and a fast fractionally encoded steady-state gradient echo sequence. NMR Biomed. 27 (7), 784–794.

Sahebjavaher, R. S., Nir, G., Honarvar, M., Gagnon, L. O., Ischia, J., Jones, E. C., Chang, S. D., Fazli, L., Goldenberg, S. L., Rohling, R., Kozlowski, P., Sinkus, R., Salcudean, S., 2015. MR elastography of prostate cancer: quantitative comparison with histopathology and repeatability of methods. NMR Biomed. 28 (1), 124–139.

Samani, A., Zubovits, J., Plewes, D., 2007. Elastic moduli of normal and pathological human breast tissues: an inversion-technique-based investigation of 169 samples. Physics in medicine and biology 52 (6), 1565.

Savitzky, A., Golay, M. J., 1964. Smoothing and differentiation of data by simplified least squares procedures. Anal. Chem. 36 (8), 1627–1639.

Schregel, K., ne Tysiak, E. W., Garteiser, P., Gemeinhardt, I., Prozorovski, T., Aktas, O., Merz, H., Petersen, D., Wuerfel, J., Sinkus, R., 2012. Demyelination reduces brain parenchymal stiffness quantified in vivo by magnetic resonance elastography. Proc. Natl. Acad. Sci. U.S.A. 109 (17), 6650–6655.

Sinkus, R., Lorenzen, J., Schrader, D., Lorenzen, M., Dargatz, M., Holz, D., 2000. High-resolution tensor mr elastography for breast tumour detection. Physics in Medicine and Biology 45 (6), 1649–1664.

Sinkus, R., Siegmann, K., Xydeas, T., Tanter, M., Claussen, C., Fink, M., 2007. MR elastography of breast lesions: understanding the solid/liquid duality can improve the specificity of contrast-enhanced MR mammography. Magn. Reson. Med. 58, 1135–1144.

ACCEPTED MANUSCRIPT

Sinkus, R., Tanter, M., Catheline, S., Lorenzen, J., Kuhl, C., Sondermann, E., Fink, M., 2005a. Imaging anisotropic and viscous properties of breast tissue by magnetic resonance-elastography. Magn. Reson. Med. 53 (2), 372–387.

Sinkus, R., Tanter, M., Xydeas, T., Catheline, S., Bercoff, J., Fink, M., 2005b. Viscoelastic shear properties of in vivo breast lesions measured by MR elastography. Magnetic Resonance Imaging 23 (2, SI), 159–165.

Tikhonov, A. N., Goncharsky, A. V., Stepanov, V. V., Yagola, A. G., 1995. Numerical Methods for the Solution of Ill-Posed Problems. Springer, Netherlands.

Tzschätzsch, H., Guo, J., Dittmann, F., Hirsch, S., Barnhill, E., Jöhrens, K., Braun, J., Sack, I., 2016. Tomoelastography by multifrequency wave number recovery from time-harmonic propagating shear waves. Medical Image Analysis 30, 1–10.

Van Houten, E. E., Miga, M. I., Weaver, J. B., Kennedy, F. E., Paulsen, K. D., 2001. Three-dimensional subzone-based reconstruction algorithm for MR elastography. Magn. Reson. Med. 45, 827–837.

Venkatesh, S. K., Yin, M., Ehman, R. L., 2013. Magnetic resonance elastography of liver: technique, analysis, and clinical applications. Journal of magnetic resonance imaging 37, 544–555.

Yeh, W. C., Li, P. C., Jeng, Y. M., Hsu, H. C., Kuo, P. L., Li, M. L., Yang, P. M., Po, H. L., 2002. Elastic modulus measurements of human liver and correlation with pathology. Ultrasound Med. Biol. 28 (4), 467–474.

Yin, M., Talwalkar, J. A., Glaser, K. J., Manduca, A., Grimm, R. C., Rossman, P. J., Fidler, J. L., Ehman, R. L., 2007. Assessment of hepatic fibrosis with magnetic resonance elastography. Clinical Gastroenterology and Hepatology 5 (10), 1207–1213.

ACCEPTED MANUSCRIPT

Zhang, Y., Hall, L. O., Goldgof, D. B., Sarkar, S., 2006. A constrained genetic approach for computing material property of elastic objects. IEEE Transactions on Evolutionary Computation 10 (3), 341–357.

Zhu, Y., Hall, T. J., Jiang, J., 2003. A finite-element approach for young's modulus reconstruction. IEEE Transactions on Medical Imaging 22 (7), 890–901.

ACCEPTED MANUSCRIPT

ACCEPTED MANUSCRIPT

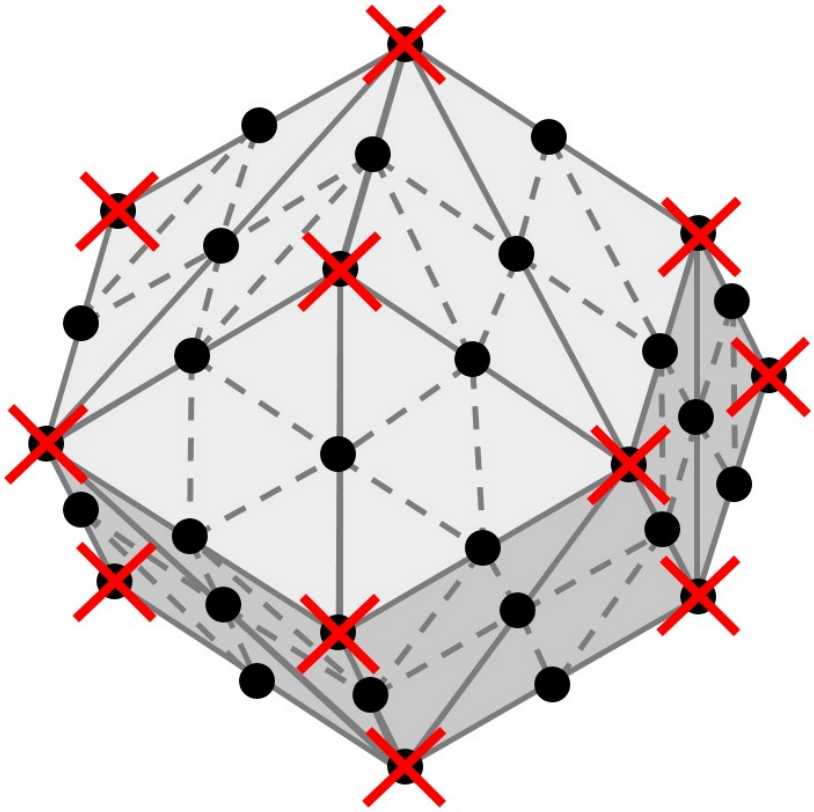

Figure 1: Tetrahedral finite element mesh centered at the current voxel. Displacement nodes are denoted by black circles and pressure nodes by red crosses. Solid lines represent the edges of the large elements and dotted lines represent the edges of the small elements (the small elements also have edges along all edges of the large elements).

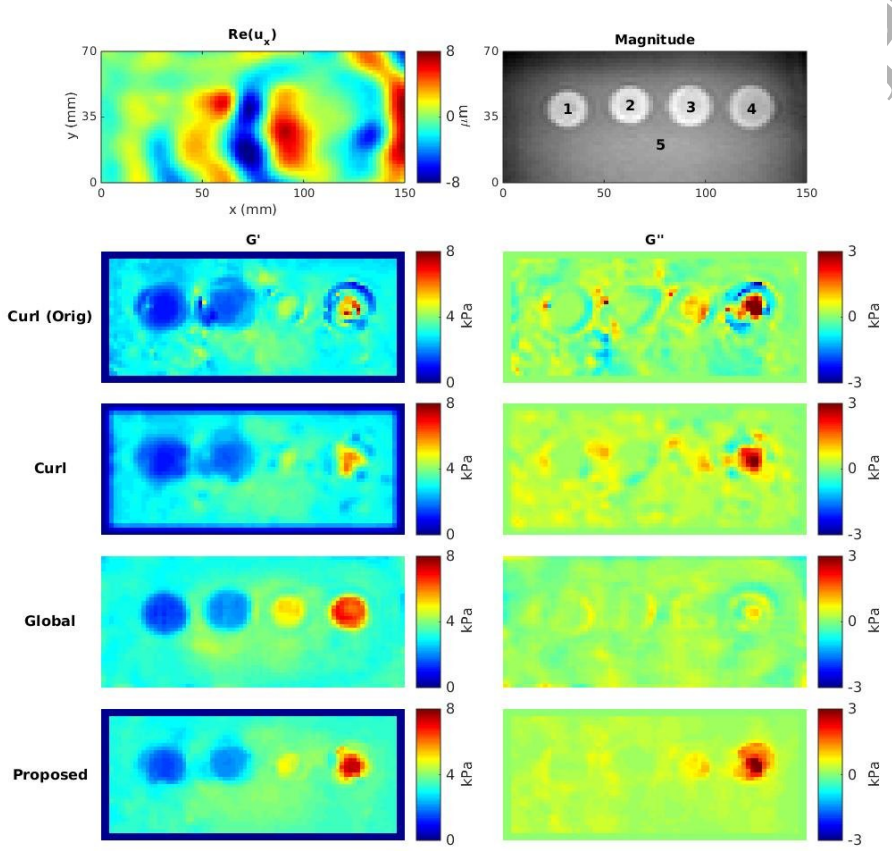

Figure 2: Reconstructions of CIRS phantom data set showing the middle slice. Left to right and top to bottom: Real x-displacements, magnitude image with five regions labeled, G' and G'' from the local curl reconstruction (both original and improved), G' and G'' from the global FEM reconstruction, G' and G'' from the proposed reconstruction.

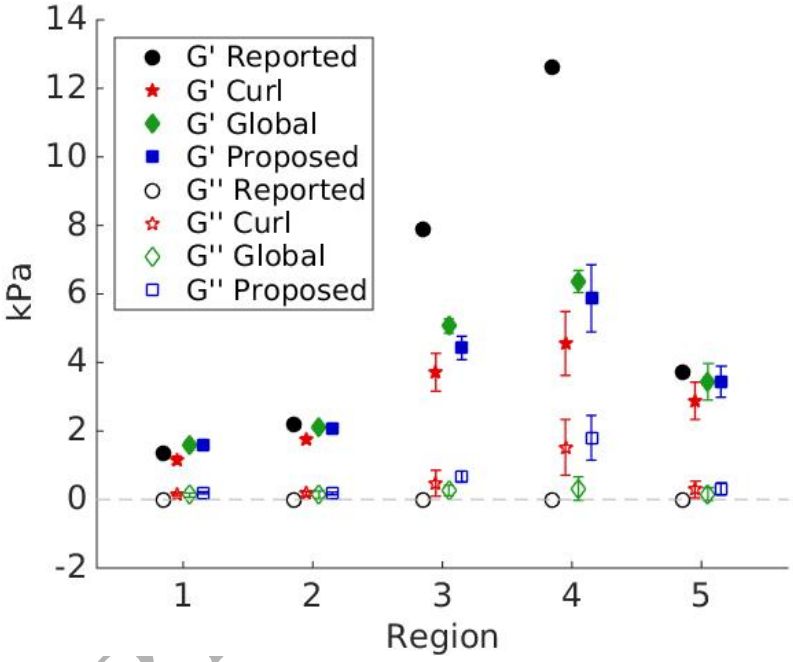

Figure 3: Means and standard deviations of G' and G'' in each of the five regions of the CIRS phantom. Reconstructed values from the local curl, global, and proposed methods are plotted against reported values.

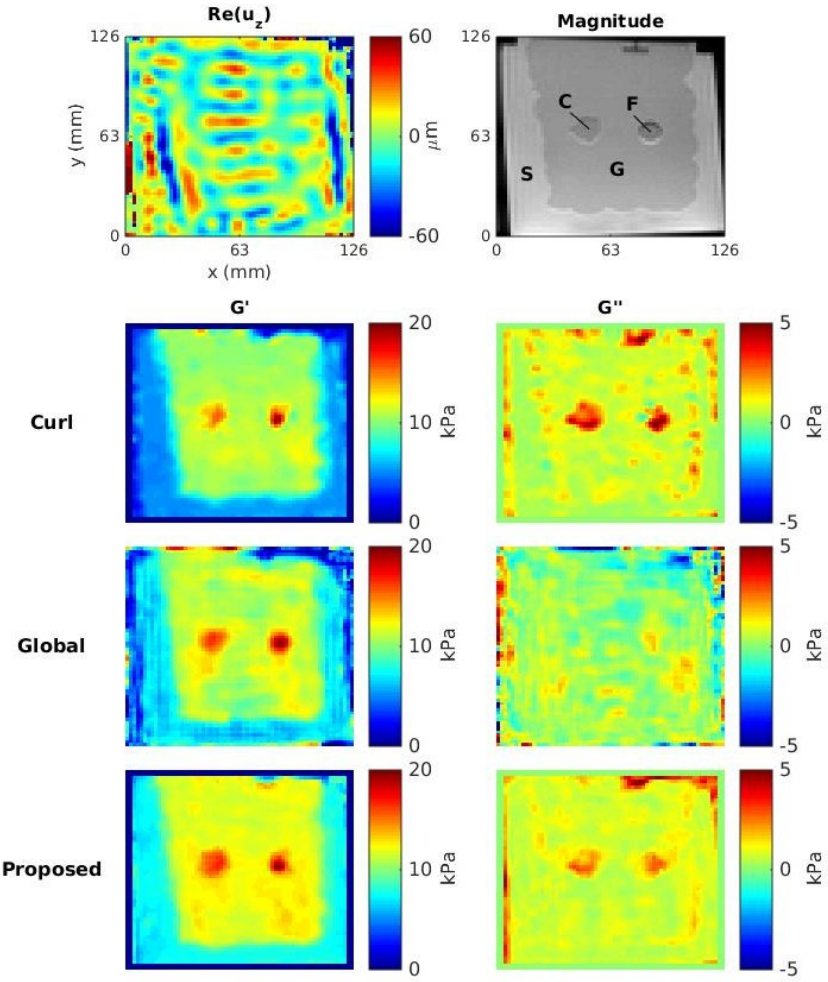

Figure 4: Reconstructions of the breast tissue phantom data set showing the middle slice. Left to right and top to bottom: Real z displacements, magnitude image with four regions labeled, G' and G'' from the local curl reconstruction, G' and G'' from the global FEM reconstruction, G' and G'' from the proposed reconstruction.

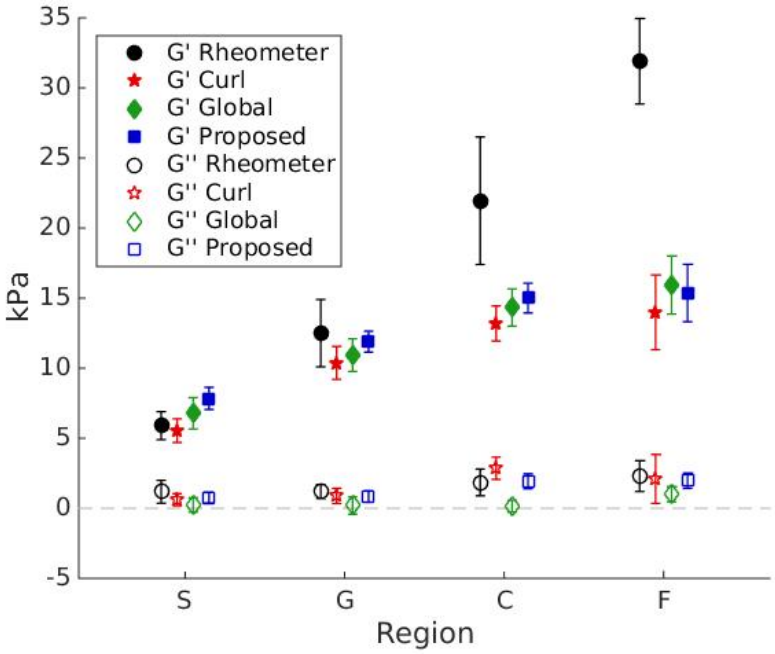

Figure 5: Means and standard deviations of G' and G'' in each of the four regions of the breast tissue phantom. Reconstructed values from the local curl, global FEM, and proposed methods are plotted against measured values.

ACCEPTED MANUSCRIPT

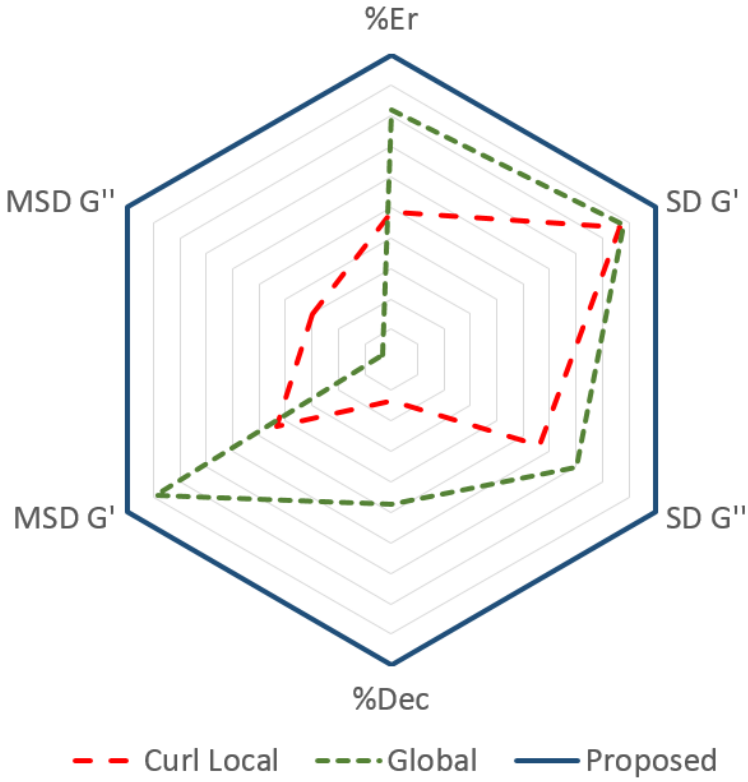

Figure 6: Spider plot showing the results of six tests performed on the CIRS phantom data which measure the effects of noise on the reconstruction methods. All three methods were tested and the best performing method's result is scaled to 1 and lies on the outer rim of the plot.

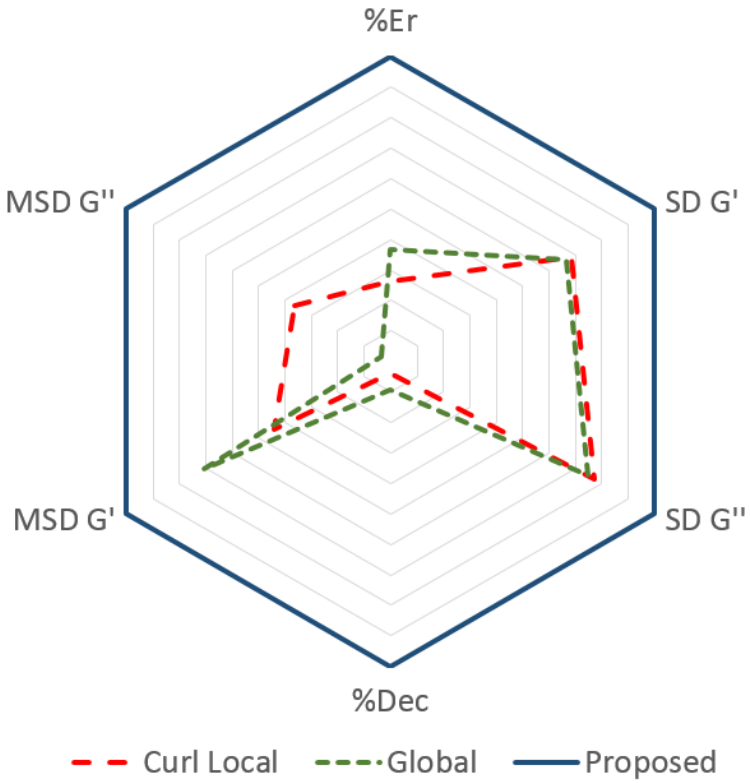

Figure 7: Spider plot showing the results of six tests performed on the breast phantom data which measure the effects of noise on the reconstruction methods. All three methods were tested and the best performing method's result is scaled to 1 and lies on the outer rim of the plot.

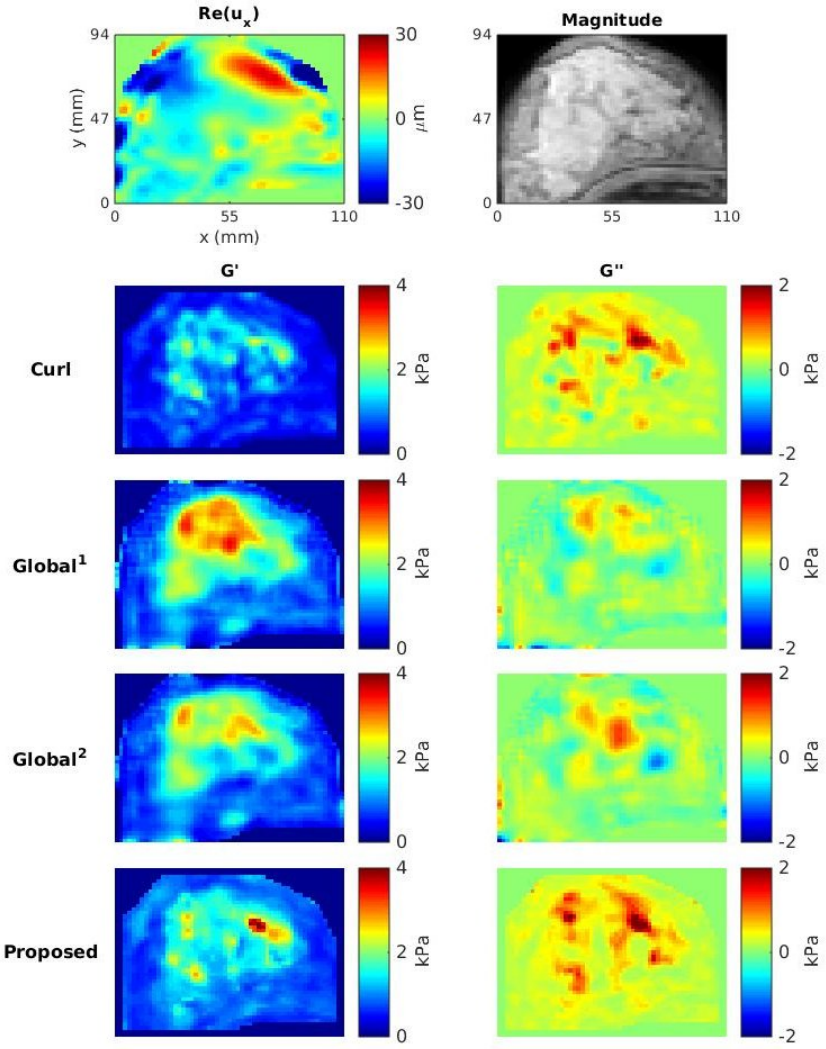

Figure 8: Reconstructions of the breast data set showing the middle slice. Left to right and top to bottom: Real x displacements, magnitude image, G' and G'' from the local curl reconstruction, G' and G'' from the global FEM reconstruction using the first set of pressure regularization parameters and then with the second set, and G' and G'' from the proposed reconstruction.

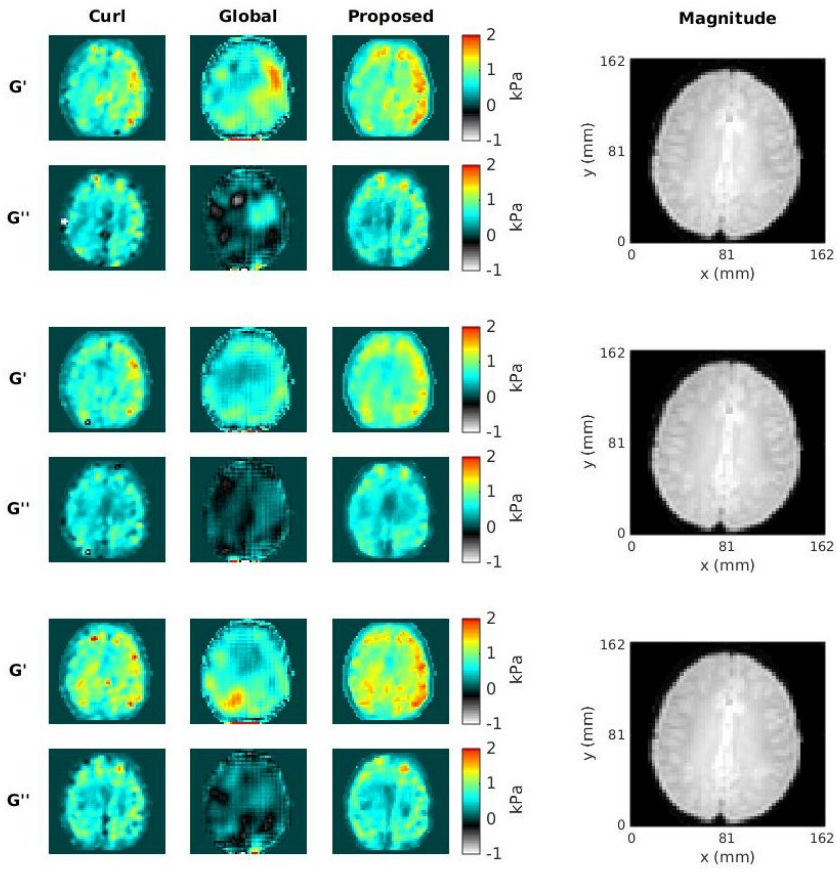

Figure 9: Reconstructions of the three brain data sets showing the middle slice. The local curl, global FEM, and proposed methods' elastograms are presented left to right followed by the corresponding magnitude image. Both G' and G'' over the three data sets are presented top to bottom.

ACCEPTED MANUSCRIPT

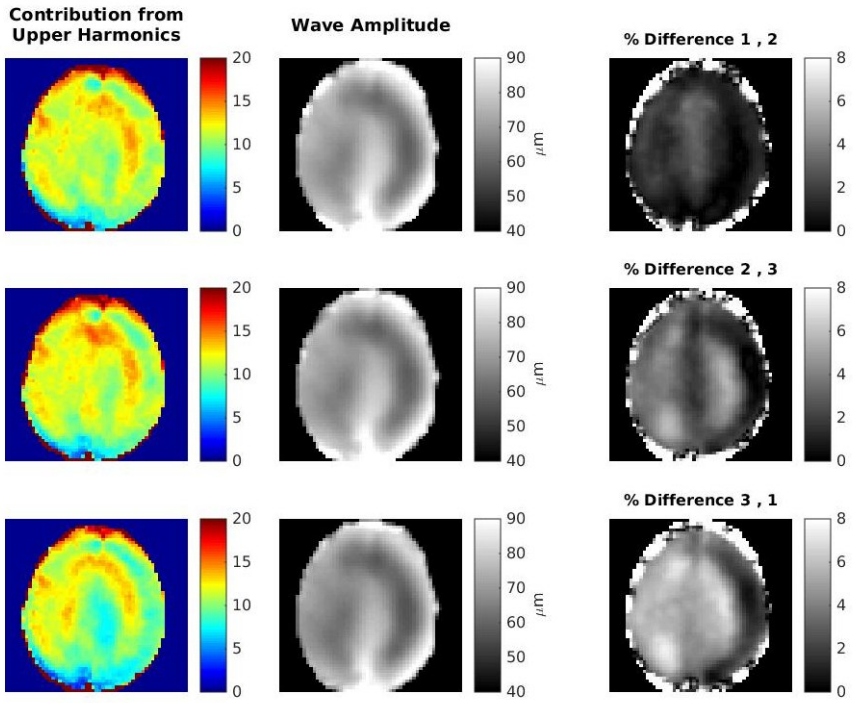

Figure 10: Additional information for the brain data sets. The percent contribution from upper harmonics (a measurement of data quality) and the amplitude of the waves are presented for the three data sets from top to bottom. On the right, the percent differences between the amplitudes for each pair of data sets are shown. For example, % Difference 1 , 2 shows the difference between the first and second data sets.

ACCEPTED MANUSCRIPT

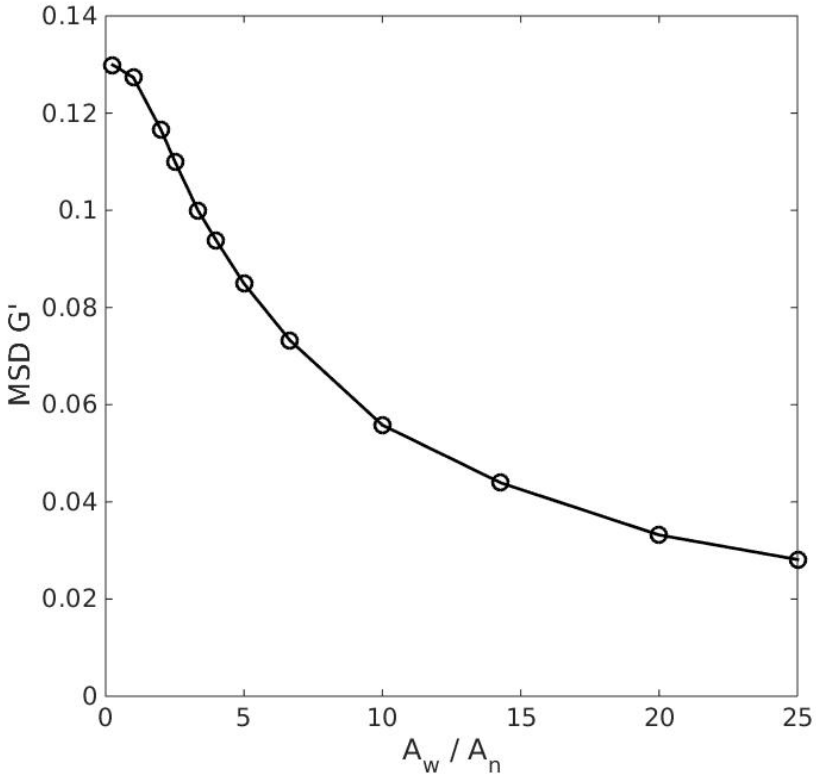

Figure 11: Plot showing the relation between the MSD (mean standard deviation) of G' and various levels of added noise for the proposed method. A_w/A_n signifies the ratio of the average wave amplitude to the noise amplitude.